Hydrothermal alteration of chromitite-dunite pairs from the Sabzevar ophiolite (NE Iran): Chemical and nano-textural evolution of Cr-spinel

Alireza Eslami, Benjamin Malvoisin, Fabrice Brunet

To cite this version:

Alireza Eslami, Benjamin Malvoisin, Fabrice Brunet. Hydrothermal alteration of chromitite-dunite pairs from the Sabzevar ophiolite (NE Iran): Chemical and nano-textural evolution of Cr-spinel. Lithos, 2023, 442-443, pp.107093. 10.1016/j.lithos.2023.107093 . hal-04300417

HAL Id: hal-04300417
https://hal.science/hal-04300417v1

Submitted on 27 Nov 2023

Hydrothermal alteration of chromitite-dunite pairs from the Sabzevar ophiolite (NE Iran): Chemical and nano-textural evolution of Cr-spinel

Alireza Eslami[1,2*], Benjamin Malvoisin[1] and Fabrice Brunet[1]

[1]ISTerre, Univ. Grenoble Alpes, Univ. Savoie Mont-Blanc, CNRS, IRD, IFSTTAR, 38041 Grenoble, France

[2]M&U sas, 38360 Sassenage, France

Abstract

Hydrothermal alteration of chromitite bodies in the form of pods (from a few centimeters to a few tens of meters in thickness) from the central sector of the Sabzevar ophiolite belt (NE Iran) was examined down to the nanoscale. The main Cr-spinel alteration feature corresponds to homogeneous cores (primary Cr-spinel) either rimmed by or locally replaced by heterogeneous domains composed of spinel grains with little or no inclusions / pores. The chemical evolution of spinel in response to hydrothermal alteration is found to follow two distinct chemical trends: (i) in the massive and semi-massive chromitites, the trend consists in the progressive increase of Cr without Fe^{3+} incorporation; (ii) in serpentinized dunites containing disseminated Cr-spinel grains, the increase in Cr occurs in conjunction with Fe^{3+} incorporation. These two trends involve a decrease in the spinel $Mg/(Mg+Fe^{2+})$ ratio. Nanoscale observation using transmission electron microscopy (TEM) shows that porous ferrian Cr-spinel which are poorer in Al and Mg and richer in Cr and Fe than the primary Cr-spinel, contains relicts of the primary Cr-spinel as well as intercalated platelets of newly formed magnetite and lizardite/chlorite. Automated crystal orientation mapping reveals that the (001) and (111) planes of newly formed lizardite/chlorite and Cr-spinel/magnetite, respectively, are parallel. The replacement of the primary Cr-spinel by porous ferrian Cr-spinel and magnetite is found to be isomorphic. The pores, ranging from 2 to 15 μm in size, may act as pathways for the aqueous solutions involved in the serpentinization process, which fed the crystallization of alteration minerals in the pores. The two different compositional trends in chromite grains from massive/semi-massive chromitite and hosted in serpentinized dunite are best explained, using mass-balance calculation, by considering the influence of the Cr-spinel/(Cr-spinel+olivine) initial ratio in the rock (X_{Chr}) and the dissolution of Mg at a water-to-rock ratio (w/r) above one. In general, at the cm-to-meter scale, Al and Fe exchange between chromitites and their serpentinized dunite envelope was not observed in the central sector of the Sabzevar ophiolite belt; however, such Al and Fe transfer is clearly observed in other parts of this ophiolite belt, where hydrothermal alteration of podiform chromitites produced magnetite ores. Comparatively, the small extend of chromitite alteration observed here, likely reflects the product of lesser fluid-rock interaction with w/r ratio close to one instead of $> 10^3$ estimated for the magnetite ores based on the magnitude of the Al transfer to their dunite envelope.

Introduction

Chromian spinel (Cr-spinel) is a common accessory mineral in igneous mafic and ultramafic rocks. Mantle section of ophiolite may host accumulation of Cr-spinel as podiform and/or stratiform bodies (*e.g.*, Augé, 1987; Lorand and Ceuleneer, 1989; Gauthier et al., 1990; Borisova et al., 2012; González-Jiménez et al., 2014; Arai and Miura, 2016; Arai, 2021). These bodies are usually separated from the host harzburgite by a dunite envelope of variable thickness from a few centimeters to several meters (e.g., González-Jiménez et al., 2014; Arai and Miura, 2016). They display massive (> 90 vol% Cr-spinel) and semi-massive (5 – 50% Cr-spinel; corresponding to serpentinized chromitiferous dunite as defined by Greenbaum, 1977) textures. Cr-spinel has been considered as a highly resistant and non-reactive mineral which tends to retain its initial magmatic composition (e.g., Burkhard, 1993; Barnes, 2000; Barnes and Roeder, 2001; Oze et al., 2004). However, hydrothermal alteration and/or metamorphism may lead to significant changes in Cr-spinel texture and chemical composition (e.g. Colás et al., 2014; Barra et al., 2014; Eslami et al., 2021; Roy et al., 2022). With respect to major elements, Cr-spinel composition evolves towards an increase in iron (Fe^{2+} and/or Fe^{3+}) and a decrease in magnesium and aluminum contents. Therefore, the spinel composition shifts towards the Cr-spinel end-member ($FeCr_2O_4$) and/or towards ferrian Cr-spinel compositions ($Cr^{3+}>Fe^{3+}>Al^{3+}$). Ferrian Cr-spinel compositions, $(Fe^{2+},Mg)Cr_2O_4$, with $Fe^{2+}>>Mg^{2+}$ and $Fe^{3+}>>Al^{3+}$ are often termed "ferritchromit" in the literature. It often occurs as rim around Cr-spinel, which evolves towards pure magnetite.

The conditions and processes of Cr-spinel alteration have been widely discussed in the literature, since the 1970s. In altered chromitites from the Stillwater complex (Montana, USA), Beeson and Jackson (1969) proposed a volume-to-volume replacement of the primary Cr-spinel by ferrian Cr-spinel at constant Cr and low Al and Mg, which is incorporated into chlorite. The prominent role of chlorite production on Mg and Al depletion in ferrian Cr-spinel with respect to the primary Cr-spinel was also outlined in the Twin Sisters dunite (Washington, USA) by Onyeagocha (1974) who, in addition, invoked an oxidation process. Furthermore, Haslam et al. (1976) described chlorite – ferrian Cr-spinel intergrowths in the serpentinized Chimwadzulu Hill peridotite (Malawi). They proposed the simplified $MgAl_2O_4$ (spinel ss) + enstatite + forsterite => Mg-chlorite reaction to account for Mg and Al removal from primary spinel. In the Pennsylvania-Maryland district, Ulmer (1974) interpreted ferrian Cr-spinel rims around the primary spinel core as a secondary overgrowth fed in Cr by the serpentinization fluid. Bliss and McLean (1975) argued that, in central Manitoba, ferrian Cr-spinel rims were produced through a metamorphic reaction between Cr-spinel core and a magnetite rim which developed during serpentinization prior to the metamorphic event. Prabhakar and Bhattacharya (2013) also interpreted ferrian Cr-spinel formation as a result of inter-crystalline diffusion between magnetite and Cr-spinel core. On the contrary, Wylie et al. (1987) ruled out the possibility of ferrian Cr-spinel rinds as a reaction zone between Cr-spinel and magnetite in the case of altered spinels from the Maryland Piedmont. These authors rather favored a dissolution – crystallization process under hydrothermal conditions.

Spinel alteration has often been characterized in serpentinized ultramafic rocks which were submitted to subsequent metamorphism (*e.g.*, Evans and Frost, 1975; Pinsent and Hirst, 1977; Burkhard, 1993). However, there is now a large number of studies which show that Cr-spinel alteration can already occur at the serpentinization stage (Spangenberg, 1943, Ulmer, 1974; Ashley, 1975; Burkhard, 1993; Khalil & El-Makky, 2009; Mukherjee et al., 2010; Barra et al., 2014; Eslami et al., 2021). At the P-T conditions of serpentinization, a miscibility gap occurs in Cr-spinels ($T < 600$ °C, Sack and Ghiorso, 1991) which are thus expected to exsolve magnetite and ferrian Cr-spinel. Actually, Mitra et al. (1992) pointed out the absence of exsolution relationship between ferrian Cr-spinel and its spinel host in samples from the Sukinda and Nuggihalli belts (India). They propose that “ferritchromitization” is actually an oxidation process with Mg and Al being expelled from the spinel to release lattice strain (e.g. Gervilla et al., 2019).

Over the years, a general scheme which is supported by thermochemical modelling, has emerged that considers the alteration of primary spinel under retrograde conditions to be a two-stage process (Gervilla et al., 2012; Barra et al., 2014; Colás et al., 2014; 2017; 2019; Eslami et al., 2021). A first step produces Fe^{3+}-poor Cr-spinel, sometimes termed ferrian Cr-spinel, through chlorite formation, possibly under reducing conditions and high silica activity (Colás et al., 2017). Mass transfer from spinel to chlorite is believed to be responsible for the formation of porous spinel textures (*e.g.*, Gervilla et al., 2012; 2019; Colás et al., 2017). A second step, at lower temperature, involves ferrian Cr-spinel moving to Fe^{3+}-rich composition which has been ascribed to an oxidizing hydrothermal event (*e.g.*, Gervilla et al., 2012, Colás et al., 2019). This two-step chemical composition change follows a typical clockwise path in the typical Al-Cr^{3+}-Fe^{3+} ternary plot.

While most inferences about the processes of Cr-spinel alteration are based on microscale observation (i.e., alteration textures from SEM images and EPMA data), some studies clearly show that nanoscale information can also be highly relevant. For example, Shen et al. (1988) showed using transmission electron microscopy (TEM) that "ferritchromite" is not a stoichiometric spinel but is rather composed of a topotaxial intergrowth of an RO phase (FeO-rich rock salt) and an R_3O_4 phase (spinel structure). Reducing conditions prevailing during serpentinization may account for the presence of the RO phase. Shen et al. (1988) were also able to show that "ferritchromite" is associated with phyllosilicates, composed of interleaving chlorite and serpentine layers which are the likely hosts for the Al and Mg released by the primary spinel to form "ferritchromite". Mellini et al. (2005) characterized, using TEM, the contact between altered spinel rims and mesh-textured lizardite. They showed that the so-called "ferritchromite" rim consists of Cr-magnetite and chlorite/lizardite layers sharing clear epitaxial orientations. Again, phase relationships between ferrian Cr-spinel and chlorite/serpentine formation was emphasized.

In order to gain insight into hydrothermal Cr-spinel alteration under retrograde conditions (lithospheric mantle exhumation and cooling), the Sabzevar ophiolite (NE Iran) is remarkable since it also hosts magnetite ores that formed at the expense of Cr-spinel (Eslami et al., 2021). Magnetite ore is mainly composed of magnetite (> 50 vol.%) embedded in a silicate matrix. Although derived from the alteration of chromitites, the magnetite ores display a Cr_2O_3 content below 1 wt.%. Despite reducing conditions associated with serpentinization, thermochemical modeling however showed that chromium was mostly insoluble and thus likely immobile. Consequently, large amounts of iron must have been transferred from the surrounding dunite to form the magnetite ores. Eslami et al. (2021) proposed that iron transfer over distances of more than 10 m occurred during serpentinization. Finally, Eslami et al. (2021) showed, on the same samples, the added-value of sub-micrometer observation to characterize the Cr-spinel – magnetite replacement processes. Indeed, ferrian Cr-spinel which, like magnetite, is a common end-product of Cr-spinel hydrothermal alteration could only be unequivocally identified using the TEM.

The Sabzevar ophiolite also hosts chromitite pods (Soleimani and Shokri, 2016) with Cr-spinel that is much less altered than magnetite ores and whose mineralogy has not yet been studied in detail. Thus, the main objective of this study is to investigate whether there is a continuum in spinel alteration between these chromitite pods and those studied by Eslami et al. (2021) which reached the magnetite ore level. Chromitites and their serpentinized dunite envelope were collected (referred to as chromitite-dunite pairs here) in order to (i) characterize Cr-spinel alteration process and (ii) track possible mass transfer from one lithology to the other. Chemical and textural evolution of altered Cr-spinel was characterized down to the nanoscale using electron microprobe analysis (EPMA) and transmission electron microscopy (TEM) in combination with an automatic crystallographic orientation tool (ASTAR™; Rauch and Véron, 2014) for the acquisition of crystal orientation maps. Finally, changes in spinel composition are interpreted in the frame of fluid - rock interactions and spinel – olivine/serpentine chemical exchange within the chromitite pods using a mass balance model based on thermochemical constraints.

Geological outline and modes of occurrence

The northern Sabzevar ophiolite belt occurs as a SE-NW trending, continuous belt for about 150 km in NE Iran (Fig. 1a), which consists of thrust-bounded blocks of Neotethyan oceanic lithosphere (Fig. 1b). Sabzevar ophiolite suit has been considered as typical tectonic ophiolite mélange (Lensch, 1980, Noghreyan, 1982, Baroz et al., 1984, Shojaat et al., 2003) which includes a complete oceanic lithospheric section (Shafaii Moghadam and Stern, 2015 and references therein). The study areas belong to the central sector of this belt (Fig. 1c), which is built by km-scale peridotite massifs, namely Kuh-Siah (Fig. 2a) and Olang-Sir (Fig. 2b). These massifs cover rugged mountainous area of ∼100 km^2 and are composed of the following ophiolitic sequence (from bottom to top): (i) a nappe of depleted mantle harzburgites with discordant dunite lenses, (ii) layered pegmatitic- and isotropic-gabbros, (iii) complex of sheeted dykes, (iv) association of marine sediments, radiolarian cherts, pelagic limestones and pillow lavas. Plagiogranite is also found as sporadic lenses within cumulate gabbro, veins/dikes crosscutting diabasic dikes and small pockets within the sheeted dike complex (Shafaii Moghadam et al., 2014). Middle Eocene dacitic domes with adakite-like composition are present to the south of these peridotite massifs. Volcanoclastic rocks and the Sabzevar ophiolitic sequences are intruded by felsic domes which are unconformably covered by Neogene-to-Quaternary deposits (Shafaii Moghadam et al., 2016).

The most common rock types in mantle section of the Sabzevar ophiolite include clinopyroxene-bearing harzburgite, harzburgite, lherzolite and dunite which are extensively serpentinized. The volumetrically dominant mantle peridotite is harzburgitic. It contains discordant dunite lenses, pyroxenitic layers and veins (Rahmani et al., 2020). All lithologies in the mantle section are cut by abundant rodingitized diabase, pegmatitic gabbro, micro-gabbro, and dykes metamorphosed under amphibolite facies conditions (Rahmani et al., 2020).

The K-Ar geochronology on amphibole~~s~~ from the lavas and diabases provided formation ages of 81.2 ± 4.1 Ma and 76.8 ± 3.8 Ma, respectively (Lensch and Davoudzadeh, 1982). Shafaii Moghadam et al. (2014) reported zircon TIMS U–Pb ages of 100, 90 and 78 Ma for three plagiogranites and faunal dates of ~ 75–68 Ma for pelagic limestones between pillows lavas throughout the northern Sabzevar ophiolite belt, indicating a drawn-out period of formation of ophiolitic sequences. In central sector of northern Sabzevar ophiolite belt, U-Pb ages on zircon (107.4 ± 2.4 Ma) and titanite (105.9 ± 2.3 Ma) in felsic segregation of mafic granulitic bodies have been interpreted as a record of peak metamorphism before the Late-Cretaceous Sabzevar back-arc basin development (Rossetti et al., 2010). The formation of the Sabzevar granulites was ascribed to subduction of the Late Jurassic–Early Cretaceous Sistan back-arc oceanic system (proto-Sabzevar Ocean) which formed earlier than the Late Cretaceous Sabzevar Ocean (Rossetti et al., 2010; Nasrabady et al., 2011).

There are large exposures of metamorphic rocks including blueschist, amphibolite and greenschist, in the northeast of the Sabzevar ophiolite belt (Fig. 1b). Radiometric K–Ar muscovite and Rb–Sr whole-rock and muscovite data of these metamorphic rocks yield an age of 54–51 Ma for amphibolite and gneiss (Omrani et al., 2013). Omrani et al. (2013) argued that these high pressure metamorphic rocks are related to north-east-dipping subduction of the Neotethys oceanic crust and subsequent closure during lower Eocene. There is no other reported evidence for high-pressure metamorphism in other parts of the Sabzevar ophiolite belt. Sea-floor alteration and low-grade metamorphism has been reported in basaltic extrusive rocks of the Sabzevar ophiolite belt (Shojaat et al., 2003).

Several chromitite bodies in the form of pods are hosted by serpentinized dunites in the Kuh-Siah and Olang-Sir massifs in the central sector of the northern Sabzevar ophiolite belt (Figs. 2a and b). The size of the chromitite bodies ranges from a few centimeters to a few tens of meters. The thickness of the dunitic envelopes around chromitites ranges from 0.5 to 3 m.

These chromitite deposits occur either as a single chromitite pod or as a series of discrete bodies. They are concordant to sub-discordant with the host peridotite foliation. A variety of chromitite textures grading from disseminated to nodular (Fig. 3a) and massive (Fig. 3b) is observed in the studied chromitite deposits. Most of these chromitite bodies are clustered along the NW-SE trending thrust fault system. Numerous NW-SE trending strike-slip faults often displace and terminate the chromitite ore bodies. The investigated ore bodies in the locus of thrust fault zone(s) show strong shearing deformation. These ore bodies are intensively folded and show mylonitic structure. In the Olang-Sir deposit, a few magnetite ore veins with massive texture are embedded in serpentinized dunite (Fig. 3c). The thickness of the magnetite ore veins varies between 2 and 5 centimeters. In the northwest of the Olang-Sir deposit, larger pod-like massive magnetite ores with average thickness of 0.5 meter, are hosted by intensely sheared and pervasively serpentinized peridotites (Eslami et al., 2021).

Materials and methods

Thirteen chromitite specimens from individual chromitite pods and nine samples from their associated host serpentinized dunite envelope were collected from nine chromitite mines in the studied area (Fig. 2).

Bulk-rock analyses for chromitite and associated dunite samples were carried out in the Service d'Analyse des Roches et des Minéraux (SARM) at the Centre de Recherches Pétrographiques et Géochimiques (Nancy, France). Major element (SiO_2, Al_2O_3, $Fe_2O_3^T$, MnO, MgO, CaO, Na_2O, K_2O, TiO_2 and P_2O_5) analyses were performed using an inductively coupled-plasma optical emission spectrometer (ICP OES iCap 6500, from ThermoFisher) and trace element (As, Ba, Be, Bi, Cd, Ce, Co, Cr, Cs, Cu, Dy, Er, Eu, Ga, Gd, Ge, Hf, Ho, In, La, Lu, Mo, Nb, Nd, Ni, Pb, Pr, Rb, Sb, Sm, Sn, Sr, Ta, Tb, Th, Tm, U, V, W, Y, Yb, Zn and Zr) compositions were measured using an inductively coupled-plasma mass-spectrometer (ICP-MS iCapQ from ThermoFisher). The samples were fused with $LiBO_2$ before being dissolved in HNO_3. Analytical uncertainty (1σ) is 5 - 25% for major elements and 5 – 20% for minor and trace elements. The Loss On Ignition (LOI) is obtained by fusion of a sample aliquot placed in an alumina crucible in an oven at 1050°C during 5 h.

Quantitative chemical analyses of individual spinel (Cr-spinel and magnetite) and silicate minerals were carried out using a JEOL JXA-8230 electron probe micro-analyzer (EPMA) equipped with five wavelength-dispersive spectrometers (WDS) and an energy-dispersive spectrometer (EDS) at the Institut des Sciences de la Terre (ISTerre), University Grenoble Alpes, France. The beam was set at an accelerating potential of 15 kV and a probe current of 100 nA and ~1 μm beam diameter. The concentrations of major elements (Fe, Cr, Al and Mg), minor and trace elements (Si, V, Ti, Ni, Co, Mn and Zn) were measured by EDS and WDS, respectively. Total counting times (peak plus background) were 440 s for Si Kα; 240 s for V Kα, Ti Kα; 360 s for Co Kα; 180 s for Zn Kα; 100 s for Ni Kα and Mn Kα. Natural minerals, pure metals and synthetic oxides were used as standards and the ZAF correction was applied. Spectral interference (V Kα vs Ti Kβ) was corrected using the JEOL software-calculated correction factor. The detection limits varied between 0.005 and 0.02 wt.%, using 3-sigma criterion (Batanova and al., 2018). Elemental distribution maps were collected using an accelerating voltage of 15 kV, a beam current of 200 nA and a dwell time of 700 ms. Iron has been assumed to be the only mixed valence element in spinel. Fe^{3+} and Fe^{2+} contents were calculated from charge balance based on three cations for four oxygens per formula unit.

Interfaces between Cr-spinels with different microstructures and compositions were examined at the nanoscale in a selected serpentinized dunite sample (sample O26, location on Fig.

5) by transmission electron microscopy (TEM). Three TEM lamellae were first extracted from a petrographic thin section across a marginal portion of Cr-spinels and thinned to < 100 nm using the focused ion beam (FIB) technique at the Institut d'Electronique, de Microélectronique et de Nanotechnologie of Lille (France). The composition at the spinel interfaces was determined by combining scanning transmission electron imaging (STEM) with EDS mapping using a Field Electron Gun JEOL^{TM} 2100F TEM operated at 200 keV (CMTC, Grenoble, France). The compositional maps acquired with this technique provide only qualitative information on the composition. The oxygen maps were used to scale the number of counts and thus correct for thickness variation. Electron diffraction patterns were also acquired with an automatic crystallographic orientation tool (ASTAR^{TM}; Rauch and Véron, 2014) with a spacing ranging from 6 to 10 nm on ~ 600 x 600 grids. A comparison of the acquired patterns with templates pre-calculated with X-ray diffraction data for lizardite, chlorite, Cr-spinel and magnetite allowed to determine the nature of each phase and its orientation.

We performed thermodynamic calculations to investigate the effect of the silicate/Cr-spinel ratio on element solubility, a crucial parameter for mass balance calculations (see discussion for details). Solubility was calculated with Perple_X software (Connolly, 2005) using the same P-T-fO_2 conditions, thermodynamic database and solid solutions as in Eslami et al. (2021). Three distinct calculations were performed using three distinct bulk-rock compositions corresponding to Cr-spinel/(olivine + Cr-spinel) fractions (X_{Chr}) of 5, 50 and 99 mol.%. The compositions of olivine and Cr-spinel were set to $(Mg_{0.92}Fe_{0.08})_2SiO_4$ and $(Mg_{0.95}Fe_{0.05})(Cr_{1.31}Al_{0.61}Fe_{0.08})O_4$, respectively, and a water-to-rock ratio of ~1 was used. As discussed in Eslami et al. (2021), the solid solution used here for spinel does not allow to reproduce the expected Mg/(Mg+Fe) ratio (Mg#) in spinel at high temperature. However, this limitation has only minor consequences on the order of magnitude of the calculated solubility, which mainly depends on the presence of a phase rather than on its precise composition.

Results

Petrological and mineralogical description

Mineralogy and texture of chromitite and associated serpentinized dunite

The Sabzevar chromitite samples are made up of massive and semi-massive chromitites. The silicate matrix is composed of serpentine and brucite which are intergrown at the submicrometer scale, leading to mixed analyses using the electron probe in most cases. Cr-spinel shows a main alteration microtexture that can be described as follows on the basis of SEM images. It corresponds to homogeneous spinel cores either rimmed by or locally replaced by heterogeneous domains composed of Cr-spinel grains with little or no inclusions / pores (Fig. 4a) or patches of porous Cr-spinel (Fig 4b-c). This textural type is mostly visible in the massive and semi-massive chromitites. Rims of porous Cr-spinel have thicknesses ranging from 15 to 250 µm. The pore size ranges from 2 to 15 µm. The pores are either empty or filled with magnetite, serpentine or chlorite (Fig. 4c). Actually, chlorite was only observed in spinel pores and not in the silicate matrix. Following the nomenclature used by Gervilla et al. (2012), this type of texture will be called *partly altered* Cr-spinel. In highly deformed chromitite bodies (i.e., sample SI-2c), partly altered Cr-spinel grains are cut by magnetite veinlets and the matrix is composed of serpentine with subordinate andradite and calcite (Fig. 4d).

Chromitite bodies are surrounded by a serpentinized dunite envelope where olivine, inferred to be initially subhedral and equigranular, is fully replaced by patches of mesh-textured serpentine/brucite intergrowths (Fig. 5a) which are 2 to 6 mm across and represent up to 95 modal percent. The serpentinized dunite also contains about 2 to 4 modal percent of anhedral to subhedral Cr-spinel (1 - 2 mm across; Fig. 5b) and accessory clinopyroxene (< 2 modal percent, 0.5 - 2 mm in size). In a few samples, clinopyroxene occurs as residual grains and/or needles intercalated with magnetite (Fig. S1). Such needles are commonly observed in serpentinized peridotites where they are interpreted as relicts of exsolution in olivine at high temperature (Malvoisin et al., 2020). Cr-spinel alteration texture as described above for the chromitite (i.e., partly altered). In one instance (sample O26), Cr-spinel has a homogeneous core rimed by a homogeneous rim of secondary spinel having a thickness of 5 to 30 µm (Fig. 5c-d). The contact between spinel core and its alteration rim is sharp (Fig. 5e). Following Gervilla et al. (2012), this type of texture will be called *zoned Cr-spinel*. It must be noted that zoned Cr-spinel texture can also display patches of porous Cr-spinel at the interface between spinel core and homogeneous rim (Fig. 5f-g). The porous Cr-spinel areas are marked by globular or elongated pores.

Silicate chemistry

Representative microprobe analyses of serpentine, serpentine/brucite mixture, spinel-hosted chlorite inclusions, andradite and clinopyroxene from the Sabzevar chromitite ore deposits are given in Tables S1, S2, S3, S4 and S5, respectively. The average composition of single serpentine grains is $(Mg_{5.55}Fe_{0.23}Al_{0.12}Cr_{0.06})_{\Sigma=5.96}Si_{3.96}O_{10}(OH)_8$ (Table S1). The Mg# $[(Mg/Mg + Fe^{2+})]$ of the serpentine/brucite mixture systematically decreases with increasing the molar fraction of brucite in the mixture (Table S2). Based on a fit of the composition of the serpentine/brucite mixture with the equations provided in Malvoisin et al. (2020), the Mg# of serpentine and brucite in the matrix are estimated to ~ 0.97 and ~ 0.82, respectively (Table S2).

Chlorite which as only been found as inclusion in Cr-spinel is categorized as clinochlore following the classification of Bailey (1980). Mg# ranges from 90 to 98 mol.%. The average composition of chlorite is $(Mg_{9.60}Al_{1.53}Cr_{0.52}Fe_{0.27})_{\Sigma=11.92}(Si_{6.05}Al_{1.95})_8O_{20}(OH)_{16}$ (Table S3).

Garnets observed in highly deformed chromitite (i.e., sample SI-2c) are andradite with average composition $Ca_{2.99}Fe_{1.85}Si_{2.90}O_{12}$ (Table S4). The Cr_2O_3 content of andradite ranges from 1.42 to 2.76 wt.%.

Clinopyroxenes in associated serpentinized dunite are diopsidic with average formula $(Na_{0.02}Ca_{0.94})_{\Sigma=0.96}(Mg_{0.93}Fe^{2+}_{0.03}Fe^{3+}_{0.02}Cr_{0.05}Al_{0.07})_{\Sigma=1.10}Si_{1.93}O_6$. They are marked by Mg# ranging between 93 and 98 mol.% (Table S5).

Spinel chemistry

The composition of spinel from chromitites and their associated serpentinized dunites is plotted in a (Fe^{3+}–Cr–Al) ternary plot (Fig. 6b-c). All these compositions correspond either to Cr-spinel or magnesiochromite according to the spinel classification proposed by Bosi et al. (2019). The composition of homogeneous spinel cores in the chromitites corresponds to magnesiochromite. It is characterized by a Cr#, [Cr/(Cr + Al)], ranging between 60 and 74 mol.% and an Mg# ranging between 61 and 71 mol.% (Table S6). Minor oxide content in these homogeneous cores is typically below 0.35 wt.% ($TiO_2 \leq 0.31$ wt.%; $MnO \leq 0.19$ wt.%; and NiO from 0.08 to 0.18 wt.%; Table S6) and generally analogous to those measured in the Cr-spinel grains from the serpentinized dunite envelope (Table S7). These compositions might depart from primary magmatic compositions since they have been likely modified during dry sub-solidus equilibration with olivine (e.g., Bussolesi et al., 2021). However, they will be called primary Cr-spinel in the following since they represent the earliest stage that is preserved. The composition of ferrian Cr-spinel formed after Cr-spinel when plotted as a function of their trivalent cation content in a ternary Al-Cr-Fe diagram (Fig. 6b), seems to follow two distinct chemical trends. "Trend 1", close to the Cr apex, is characterized by Cr progressively increasing from the primary composition. This trend is discernible in semi-massive and massive chromitites. The structural formula of ferrian Cr-spinel from this trend is $(Fe_{0.30-0.84}, Mg_{0.13-0.70})(Cr_{1.22-1.79}, Al_{0.02-0.68},Fe^{3+}_{0-0.59})O_4$. "Trend 2" shows an increase in Cr coupled to an increase in total iron compared to "Trend 1" (Fig. 6b). This latter trend is related to ferrian Cr-spinel $(Fe_{0.55-0.75}, Mg_{0.23-0.44})(Cr_{1.21-1.46},Al_{0.26-0.49},Fe^{3+}_{0.17-0.48})O_4$ with porous texture in a serpentinized dunite with disseminated Cr-spinel grains and in serpentinized dunite samples. For both trends, total iron (Fig. 6c) increases whereas Mg# (Fig. 6d) decreases during spinel alteration. These two distinct trends are displayed in Figures 7a and 7b. In Cr-spinel from serpentinized dunites, NiO gradually increases with alteration (Fig. 7c).

The composition of homogeneous rim around Cr-spinel in zoned Cr-spinel plots in the same area ascribed to porous Fe-Cr-spinel in the Sabzevar highly altered occurrence(s) (Eslami et al. 2021) and is marked by an Mg# between 37 and 44 mol.% and a Cr# between 63 and 73 mol.% (Table S7). Heterogeneous portions of Cr-spinel in a serpentinized dunite with disseminated Cr-spinel grains and massive chromitites plot in the areas assigned to porous Fe-Cr-spinel and homogeneous Fe-Cr-spinel, respectively (Fig. 6b). They have Cr# values ranging from 62 to 100 mol.%, and Mg# from 12 to 70 mol.% (Table S7). There is a positive correlation between Cr# and Mg#. In the serpentinized dunite (sample O26) where we cut three FIB sections, the structural formula of homogeneous corona surrounding primary Cr-spinel is $(Fe_{0.55}, Mg_{0.44})(Cr_{1.3},Al_{0.57},Fe^{3+}_{0.12})O_4$ which plots in the field of porous ferrian Cr-spinel (Fig. 6b).

Bulk-rock chemistry and mineral modes

Whole-rock geochemical analyses from the collected chromitite – host serpentinized dunite pairs along with those of three serpentinized dunites hosting magnetite ores from Eslami et al. (2021) are listed in Table S8 and S9 and displayed in Figure 8.

The composition of the massive and semi-massive chromitites and the serpentinized dunites containing disseminated grains are aligned on a mixing line between a SiO_2-free composition

(SiO_2 content below detection limit in massive chromitite) and a Cr_2O_3- and Al_2O_3-free composition (Fig. 8a). Moreover, the Al_2O_3 and Fe_2O_3 contents of the serpentinized peridotites increase with Cr_2O_3 content (Fig. 8b, 8c). This supports a bimineralic assumption, in which the bulk rock composition can be simply expressed as a mix between olivine (Mg# = 92 - 93) and Cr-spinel along with 15 to 19 wt.% of water (see also the *Mineral modes calculation* section for a validation of this model). Based on this assumption, the serpentinized ultramafic rocks which host the studied chromitites can be considered as former dunites. The high LOI values in serpentinized dunite samples (14.89 - 18.69 wt.%) indicate pervasive serpentinization. LOI and Ni-content (< 0.25 wt.%) in serpentinized dunites are correlated to SiO_2 indicating that the Ni-bearing silicate matrix is hydrated (Table S8). Extrapolation of the serpentinized dunite composition down to the Cr_2O_3 free composition (i.e., with virtually no spinel) allows to retrieve the Al_2O_3 and Fe_2O_3 contents of the original dunite (i.e., olivine) composition which amount to 0 and 7 wt.%, respectively. Serpentinized dunite which hosts magnetite ores (Fig. 8b), follows the same type of trend but about 0.3 wt.% of the bulk Al_2O_3 cannot be accounted for by spinel. Sample O24 collected near a chromitite is the only one studied here which also displays an enrichment in Al_2O_3. In the Fe_2O_3 vs. Cr_2O_3 diagram (Fig. 8b), extrapolation of serpentinized dunite compositions down to $Cr_2O_3 = 0$ yields 7 wt.% Fe_2O_3 which is consistent with a dunite composed of pure Fo92 olivine. On the other hand, the same extrapolation for serpentinized dunite hosting magnetite ores (samples MG16, MG20 and MG21; Eslami et al. 2021) yields a former dunite composed of Fo94. This also appears on Figure 8a where the samples of Eslami et al. (2021) plot at a higher SiO_2/Fe_2O_3 ratio than the serpentinized dunites of this study. It must be noted that serpentinized dunite sample O1 which was collected near a magnetite vein (Fig. 3c) also displays a relative MgO enrichment (Fig. 8c). Bulk chromitite chemistry can also be observed in Fig. 8a as one end-member on the bimineralic mixing line. Fe_2O_3 and Cr_2O_3 contents range from 8.6 and 24.6 %, and from 6.5 to 59.3 %, respectively. TiO_2 in massive chromitites is close to 0.10 - 0.15 wt.% and relatively constant whatever the chromitite texture. Among trace and minor elements which are hosted by Cr-spinel, Ga < 25 ppm, As < 500 ppm, V < 900 ppm, Zn < 1500 ppm and Mn < 2700 ppm. Samples with high Cr-spinel/silicate ratios show higher Zn, Co and V contents (Fig. 9a-c).

Mineral modes calculation

Assuming that, prior to serpentinization, the dunite was exclusively composed of olivine and Cr-spinel, the respective modes of these two minerals prior to serpentinization were retrieved by least squares regression (LSQ) through the bulk composition of the serpentinized dunite samples (Table 1). The Cr-spinel composition used in the regression was fixed based on the electron microprobe data obtained on primary Cr-spinel cores. The regression was thus performed with two variables, Mg# in olivine and the spinel molar fraction in the former spinel - olivine assemblage. Variations in Cr-spinel composition observed with the electron microprobe have little effect on the calculated modes due to the lower content of spinel in serpentinized dunite. Recalculation of the bulk oxide content from these modes leads to deviation below 1.5 wt.% on each oxide, except for sample SI-2b whose deviation reaches up to 3 wt.%.

Mineral mode calculation (Table 2) was also performed on semi-massive and a serpentinized dunite with disseminated Cr-spinel grains assuming again olivine and spinel as the only rock-forming minerals. The bulk SiO_2 content in massive chromitites is below 3 wt.% and Mg# for olivine could not be accurately retrieved. Therefore, four samples (O3, IM-1b, O27 and EB4) were considered as composed of Cr-spinel only and modes were not calculated. For the other chromitite samples, recalculation of the bulk composition with the retrieved modes led to deviations below 1.5 wt.% from the analyzed bulk-rock oxide content. The approximation of isochemical serpentinization of an initial dunitic matrix is thus supported.

Spinel alteration textures at the nanoscale

In order to resolve spinel alteration and replacement processes at the nanoscale, three FIB lamellae were cut in serpentinized dunite sample O26 across the interface between homogeneous primary Cr-spinel cores and their alteration rims (blue thick lines in Fig. 5) including a secondary homogeneous rim and patches of porous Cr-spinel. Sample O26 was actually selected for TEM studies because it contains the two types of alteration texture (partly altered and zoned Cr-spinels), with homogeneous rim and pores, encountered in the spinel grains observed in this study.

Three compositional maps (S2-A1, S2-A2 and S3-A2) were collected at the interface between homogeneous Cr-spinel and a secondary porous Fe-Cr-spinel zone (Fig. 10). The maps show that Cr-spinel in the porous zone is chemically distinct from primary Cr-spinel. It is characterized by higher Cr and Fe as well as lower Al and Mg contents, according to the chemical composition obtained by EPMA (see details below; Fig. 10). Whereas Cr-spinel is devoid of mineral inclusions, Fe-Cr-spinel in the porous zone contains pores filled with intercalated platelets of magnetite and silicates (S2-A1 and S3-A2). The silicates display fine cleavage planes consistent with layered silicate minerals. Based on the Fe-poor and Mg- and Si-rich composition and on the presence of Al, these silicates could either consist in serpentine (consistent with lizardite diffraction pattern) or chlorite with platy shapes and perfect cleavage along the (001) plane (Fig. 11e-g). Electron diffraction pattern matching indicates the co-existence of these two phases (Fig. 11). However, the phase identification reliability is low, which does not allow to unequivocally conclude on the nature of the silicate inclusions. At the nanometer scale, remnants of pristine ~1 μm-wide Cr-spinel are observed as irregular selvages in porous Fe-Cr-spinel (Fig. 10). Automated crystal orientation mapping (Fig. 11a-c) shows epitaxial growth of porous Fe-Cr-spinel from Cr-spinel. Similar epitaxial relationship is observed between magnetite and porous Cr-spinel (Fig. 11a-b). A crystallographic relationship between lizardite/chlorite and Cr-spinel/magnetite is also observed with the (001) phyllosilicate plane being parallel to the (111) Cr-spinel/magnetite plane (Fig. 11e-g). Magnetite can occur as elongated plane in between (001) phyllosilicate planes (reference to S3-A2).

Another elemental map (S3-A1) has been collected at the interface between the rim of a zoned Cr-spinel and the porous Cr-spinel area described above (Fig. 10). The pores have a rounded shape (below 1 μm across) and are distinct from the elongated pores filled with phyllosilicates (Fig. 11d). Both Cr-spinel homogeneous rim and porous area result from the alteration/replacement of Cr-spinel but it cannot be deduced from SEM images which of the two formed first. Alteration rim of zoned Cr-spinel texture is texturally homogenous since it is devoid of pores.

Cr-spinel in the porous zone and homogeneous alteration rim (zoned Cr-spinel) are characterized by higher Fe and Cr and lower Al than the Cr-spinel core in agreement with the chemical alteration trend outlined on Fig. 6. The homogeneous Cr-spinel rim contains however lower Cr and Fe and higher Al than ferrian Cr-spinel in the porous area. Despite the slight chemical differences between these two spinel textural types, they plot in the same region of the Cr-Al-Fe^{3+} diagram (Fig. 6b). Again, both types of secondary spinel share similar crystallographic orientation which is inherited from Cr-spinel, indicating topotaxial replacement.

Discussion

Cr-spinel chemical evolution during alteration

Two types of spinel chemical evolution are observed in samples from the Sabzevar ophiolite (Fig. 6b). The first trend (Trend 1) is measured in massive and semi-massive chromitites. This trend is mainly characterized by a progressive decrease in aluminum displacing spinel composition towards the $(Mg,Fe)Cr_2O_4$ end-member (Fig. 6b). The second trend (Trend 2) is measured in a serpentinized dunite with disseminated Cr-spinel grains as well as in the serpentinized dunite envelope around massive and semi-massive chromitites. It also involves aluminum removal but this removal occurs concurrently with Fe^{3+} incorporation in spinel (Fig. 6b). The final part of the two trends is similar, it involves the formation of two different spinels, one of which is close to the $FeCr_2O_4$ end-member and the other close to magnetite, Fe_3O_4. The two trends involve a decrease in Mg# (Fig 6d). However, the value of the Mg# for a given Cr# is systematically lower in a serpentinized dunite with disseminated Cr-spinel/serpentinized dunites than in massive chromitites, leading to two parallel trends in Cr# vs. Mg# diagram (Fig. 7a). Each of these two chemical trends encompasses different alteration stages (see discussion below) and is not associated to a given alteration texture. These two trends can also be observed in spinel chemical data from chromitite and host serpentinite provided in previous studies (González-Jiménez et al., 2009; Barra et al., 2014). Grieco et al. (2018) showed that the silicate/chromite ratio was a main parameter influencing Cr-spinel and olivine compositional variations during dry subsolidus re-equilibration. However, the role of this parameter on spinel chemistry has not been investigated for the hydrothermal alteration stage.

Sabzevar ophiolite in the studied area did not encounter noticeable metamorphic overprint after exhumation/obduction. Following Eslami et al. (2021), it will be considered here that Cr-spinel chemical evolution mainly proceeded upon exhumation/cooling. Thermodynamic modeling of the mineralogical evolution of the dunite envelope around magnetite ores in presence of aqueous fluid (Eslami et al., 2021) predicts that during cooling, Cr-spinel composition evolves due first to chlorite formation at temperatures below ~725°C and then to serpentine formation at temperatures below 550 °C, in good agreement with previous studies (Mellini et al., 2005; Grieco and Merlini, 2011; Gervilla et al., 2012). This alteration in two steps produces first Fe^{2+}-rich and Al-poor Cr-spinel which evolves in a second stage towards Fe^{3+}-rich spinel (Colás et al. 2019 and references therein). However, thermodynamic modeling is unable to reproduce the two trends observed here for several reasons. First, the chlorite solid-solution available in the thermochemical database does not include Cr which plays a key role regarding the evolution of spinel composition. Secondly, the spinel solid-solution used in Eslami et al. (2021) predicts a Mg# that is systematically higher than the measured one, especially at temperature above ~700°C. Last but not least, the model assumes equilibrium at the bulk-rock scale which is obviously not the case. Indeed, in the studied samples, only a small fraction of Cr-spinel has reacted and equilibrium has been reached only locally at the microscale. To circumvent these issues and determine the factors responsible for the two observed trends, we built a mass balance model based on the two successive reactions predicted by previous thermodynamic modeling. One reaction corresponds to the formation of chlorite and the other one to serpentine formation. This mass balance model is detailed in the Supplementary Materials. It considers mass transfer between the silicate matrix and Cr-spinel through a main constitutive equation recalled below (Eq.1).

The bulk-rock minus spinel compositions measured in serpentinized dunite and chromitite bodies are consistent with an olivine composition with no significant Al_2O_3 and, thus, no significant orthopyroxene. The presence of serpentine/brucite intergrowths and the absence of bastite confirm that those rocks did not contain any significant orthopyroxene, which was therefore not considered in the model. Based on the thermodynamic calculation detailed in Eslami et al. (2021), the retrograde reaction of a Cr-spinel + olivine assemblage is expected to form chlorite and then serpentine as the temperature decreases. In addition to these phases, brucite, $(Mg,Fe)(OH)_2$ and aqueous species have been proposed to be involved in similar chlorite- and serpentine-forming reactions (e.g., Gervilla et al., 2012; Barra et al., 2014; Colas et al., 2017). The formation of brucite occurs at temperatures below 400°C for which there is a miscibility gap between magnetite and Cr-bearing spinel (Sack and Ghiorso, 1991; Eslami et al., 2021). The composition of Sabzevar Cr-spinels falls in the miscible region, suggesting that alteration occurred at $T > 400°C$ (i.e., outside the stability field of brucite). Hence, this latter phase was not considered either in the thermodynamic calculations.

For the thermodynamic calculations performed here, the aqueous species concentrations are comprised between ~ 10^{-4} and 10^{-1} mol/kg for silica, 10^{-5} and 10^{-2} mol/kg for iron and 10^{-2} and

$10^{0.5}$ mol/kg for magnesium (Fig. S2). The thermodynamic model thus predicts that Mg is several orders of magnitude more soluble than Fe and Si during ultramafic rocks alteration in the 500 - 800°C temperature range. We therefore considered aqueous Mg as a potential reaction product in the spinel alteration reaction. The solubility of Mg was fixed to $10^{-0.5}$ mol/kg that is at an intermediate value between the two extreme values calculated with thermodynamic modelling (Fig. S2). The total amount of aqueous Mg (Mg^{2+}_{aq}) thus depends on the w/r ratio.

Considering Mg^{2+}_{aq} formation (Mg dissolution), spinel reaction in the presence of olivine leading to chlorite and serpentine formation can be written in a simplified form as:

Cr-spinel + Olivine + H_2O + O_2 = Fe-Cr-spinel + Chlorite + Mg^{2+},aq + Serpentine + OH^- (Eq. 1)

Chlorite formation in Eq. 1 occurs at temperatures below 725°C, that is at higher temperature than serpentine formation below 550°C (Eslami et al., 2021). The formation of serpentine in the mass balance model is thus only allowed if silica is left after chlorite formation. The effect of two parameters on spinel composition evolution is investigated: (1) the Cr-spinel fraction in the chromitite ($X_{Chr} = n_{Chr} / (n_{Chr} + n_{ol})$) where n_{Chr} and n_{ol} are the number of moles of Cr-spinel and olivine in the reacting mineralogical assemblage; (2) the water to rock ratio (w/r ratio) which fixes the amount of aqueous Mg in the reaction products of Eq. 1. The mass balance model considers spinel composition evolution for different reaction progresses (ξ). ξ is defined as the amount of olivine having reacted with spinel (n_{olr}) relative to the initial amount of olivine in the matrix, n_{ol} ($\xi = n_{olr} / n_{ol}$ and varies from 0 to 1). The mass balance model considers the progressive addition of fluid and olivine to the system. This model produces a decrease in Al content in spinel accompanied by an increase in Fe^{3+} content leading to a constant Cr^{3+} trend (Trend 2) in the Al-Cr^{3+}-Fe^{3+} diagram for a low water to rock ratio (<1; Fig. 12). The spinel compositions measured in Sabzevar massive chromitites which show a decrease in Al without increase in Fe^{3+} (Trend 1) can be reproduced with the present mass balance model by independently varying two parameters: (1) increasing the w/r ratio (Fig. 12a); (2) decreasing X_{Chr} with a fixed high water to rock ratio (Fig. 12b). The decrease in Fe^{3+} in the spinel occurs concurrently to a decrease of the Mg#. Iron is indeed the only major element present in the studied spinel with two oxidation states. It is thus able to accommodate release/uptake of magnesium in spinel through the following reaction:

$$3\ \mathrm{Mg}((\mathrm{Al,Cr})_{2/3}\mathrm{Fe}^{3+}{}_{1/3})_2\mathrm{O}_4 + 3\ \mathrm{H_2O} = 2\ \mathrm{Fe}^{2+}(\mathrm{Al,Cr})_2\mathrm{O}_4 + 3\ \mathrm{Mg}^{2+}{,}\mathrm{aq} + 6\ \mathrm{OH}^- + \tfrac{1}{2}\ \mathrm{O}_2 \quad \text{(Eq. 2)}$$

Equation 2 indicates that the fate of magnesium during alteration controls the Fe^{3+} content in spinel. Modifying X_{Chr} or the w/r ratio are two different ways of modifying Mg distribution during alteration in the mass balance model (Fig. 12). Favoring aqueous magnesium formation by increasing the w/r triggers the reaction of Eq. 2 from left to right. Figure 12a shows that a w/r above 1 can result in Trend 1.

For a fixed w/r above 1, Trend 1 can also be reproduced by increasing the amount of spinel in the reactants (X_{Chr}; Fig. 12b). The source of aqueous Mg according to the reaction of Eq. 1 is either spinel reacting through Eq. 2 from left to right, or olivine releasing excess Mg while forming chlorite and serpentine since the (Mg+Fe)/Si ratio in olivine is of 2 whereas it is of 5/3 and 3/2 in chlorite and serpentine, respectively. As a result, high X_{Chr} in the rock promotes changes in spinel composition during Mg release and Fe^{3+} decrease. However, at low X_{Chr}, aqueous Mg formation is controlled by olivine reaction involving less changes in spinel composition as a result of hydrothermal alteration.

According to the present mass balance model, the observation of both spinel chemical Trend 1 and Trend 2 could be explained by either (i) w/r variations over several orders of magnitude, or (ii) X_{Chr} variation in the presence of fluid (high w/r). (i) would imply w/r variations at the meter scale, which is not supported by the observation since no preferential fluid pathways are observed in massive chromitites. However, (ii) is compatible with the observation of Trend 2 in the dunite (low X_{Chr}) and of Trend 1 in the massive chromitites from Sabzevar (high X_{Chr}). As a result, the variation of Cr-spinel-to-silicate ratio appears to be the main factor controlling spinel composition evolution during alteration. This is only effective at high w/r (> 1) where the total amount of dissolved Mg is high ($> 10^{-0.5}$ mol/kg of rock).

The present mass balance model reproduces the two trends depicted in the Al – Cr^{3+}– Fe^{3+} ternary diagram (Fig. 6b). We show that X_{Chr} controls the evolution of the spinel composition in water-bearing systems where hydrous silicates can form. However, the mass balance model does not explain the systematic difference in Mg# at a given Cr# observed in Figure 7a at the onset of the two trends. Thus, alteration alone with chlorite and serpentine formation cannot account for this difference. Actually, X_{Chr} has been pointed out as a main parameter that controls Cr-spinel: olivine re-equilibration upon cooling in dry systems (*e.g.*, Engi, 1984, Grieco et al., 2018). Therefore, we have modeled the evolution with temperature of the Mg# of both olivine and spinel in a serpentinized dunite (sample IM-2; Table 1) and a chromitite (sample KE-2; Table 2) of contrasted X_{chr}. For this calculation, X_{chr} was deduced from mineral modes retrieved by LSQ regression. The composition of primary Cr-spinel cores obtained with EPMA were used for the computation and Cr# was set as constant.

Owing to the low Cr-spinel content (0.7 wt. %) in the serpentinized dunite, Fe-Mg exchange between olivine and Cr-spinel upon cooling does not affect the olivine composition. Therefore, reconstructed olivine compositions were tentatively used to infer equilibration temperature with spinel using the thermometer calibrated by Ballhaus et al. (1991). Temperatures in the 500 - 750 °C range were obtained which likely reflect the blocking temperature of the Fe-Mg exchange (Bussolesi et al., 2022). This temperature estimate may be hampered by the formation of Mg-chlorite which is expected to form at $T < 700$ °C according to Eslami et al. (2021). In the chromitite sample (KE-2), Fe-Mg exchange between Cr-spinel and olivine upon cooling is expected to strongly affect the olivine Mg# (Engi, 1984) which is a minor component in these samples. The Mg# of the initial olivine could be reliably retrieved for samples with SiO_2 content above 3 wt.% and was found to range between 0.92 and 0.94. From these Mg#'s and primary Cr-spinel core compositions, temperature comprised between 900 and 1080°C could be derived with the Ballhaus et al. (1991) thermometer.

In the ca. 1100 – 700 °C cooling temperature range, Cr-spinel Mg# is calculated to decrease from 0.69 down to 0.65 for the chromitite sample whereas it must decrease from 0.69 down to 0.55 for the serpentinized dunite sample. Therefore, the shift in Mg# of +1 unit at the onset of Trend 2 with respect to Trend 1 can merely be explained by the effect of sub-solidus re-equilibration for rocks having contrasted X_{chr} (i.e., chromitite vs dunite, respectively).

Cr-spinel alteration, chromitite pods vs magnetite ores

In comparison to the magnetite ores found in the same area from the Sabzevar ophiolite (Eslami et al., 2021), the studied chromitite samples show much less alteration. In particular, magnetite is an accessory phase which mostly occurs as fillings in micrometer-sized cracks. The lesser extent of alteration led to textures which significantly differ from those observed in Cr-spinel from the magnetite ores and their serpentinized dunite envelope. In particular, although both magnetite-serpentinite and chromitite-serpentinized dunite occurrences have Cr-spinel grains with partly altered textures, Cr-spinels in serpentinized dunite in the vicinity of magnetite ores are more extensively replaced leading, in some instances, to fully porous Cr-spinel grains where the primary Cr-spinel is no longer visible. Therefore, the hydrothermal alteration process should be regarded at the scale of both the Cr-spinel and its serpentinized dunite envelope. This is not only evidenced by the Cr-spinel alteration textures but also by the composition of the serpentinized dunite envelope. Eslami et al., (2021) showed that iron was transferred from the surrounding (serpentinized) dunite to the chromitite in order to form the magnetite ore. No such iron transfer can be inferred here from the iron content of the serpentinized dunite around the chromitite pods (Figs. 8a and 8c) indicating, again, that hydrothermal alteration has been less efficient and/or occurred at a smaller scale.

Possible aluminum transfer from chromitite to surrounding ultramafic rock upon hydrothermal can be argued from Fig. 8a, where ca. 0.3 wt.% of Al_2O_3 (Fig. 8a) in the dunite around the magnetite ores is unrelated to Cr-spinel.

Since olivine can barely contain more than 1000 ppm Al_2O_3 (Sobolev et al., 2007; Coogan et al., 2014), and the scarcity of bastite suggests small orthopyroxene content, if any, in the protolith (Eslami et al., 2021), Al was probably added in the course of later fluid – rock interaction (e.g., serpentinization). Indeed Al-transfer from chromitite pods under dry sub-solidus re-equilibration (at temperature higher than that of chlorite formation, i.e., > 700 °C) is unlikely since Al has been showed to be retained in spinel during such high-T sub-solidus re-equilibration (Rassios and Kostopoulos, 1990).

Figure 8a allows to subtract the contribution of Cr-spinel to Al content in the serpentinized dunites to estimate that chlorite formation corresponds to a gain of 0.3 wt.% of Al_2O_3 (C_{dun}). This mass transfer probably occurred during chromitite reaction to form the magnetitites. The magnetite pods are ~ 0.5 m thick (L_{ore}) and the Al_2O_3 concentration measured in slightly altered massive chromitite is of ~ 12 wt.% (C_{chr}). Assuming that the volume of the chromitite leading to magnetitite formation is similar to the volume of the ore, the distance of Al transport in serpentinized dunite from the chromitite (L_{dun}) can be calculated as: $L_{dun} = \frac{\rho_{chr} L_{ore} C_{chr}}{\rho_{dun} C_{dun}}$ where ρ_{chr} and ρ_{dun} are the densities of the Cr-spinel and the serpentinized dunite, respectively (4800 and 2700 kg/m^3, respectively; Chichagov et al., 2001). L_{dun} value calculated with the values given above is of ~ 40 m. This value is close to the value of ~ 30 m calculated in Eslami et al. (2021) for Fe transfer from the serpentinized dunite to the same magnetite pods. This suggests mass transfer promoted by an efficient transport mechanism during alteration. For example, the low solubility of aluminium calculated with thermodynamic calculations (10^{-7} to 10^{-4} mol/kg) implies high water to rock ratios comprised between 10^3 and 10^6 to reach by advection the measured Al concentrations measured in the serpentinized dunites near magnetitites. At the scale of chromitite pods and its dunite envelope, alteration has been much less efficient than in the localities where magnetite ores were formed. Since alteration of Cr-spinel involves the formation of hydrous phases (chlorite and serpentine) and thus, hydrothermal conditions, differences in w/r, deformation and access to the fluid, fluid composition or alteration temperatures can be invoked to account for the contrasted level of Cr-spinel alteration. The presence of a higher density of shear and fracture zones near the magnetite ores than near the chromitite pods may explain the observed difference in mass transfer (Fig. 2c).

Cr-spinel alteration processes at the nanoscale

Nanoscale observation using TEM provides valuable information on the alteration processes thanks, in particular, to the crystallographic information provided by electron diffraction. In particular, it has been showed that spinel alteration into ferrian Cr-spinel and magnetite can involve topotactic intergrowth (Shen et al., 1988) or epitaxial replacement (Eslami et al., 2021). Fleet et al. (1993) and Mellini et al. (2005) showed that even layered silicates involved in ferrian Cr-spinel and Cr-magnetite formation from spinel share crystallographic relationships with their ferrian Cr-spinel or Cr-magnetite host. Actually, they reported that the layers with the closest-packed anions in chlorite / lizardite, (001) planes, and in ferrian Cr-spinel and Cr-magnetite, (111) planes, are parallel. The same crystallographic relationship has been found here between layered silicates

(Liz/Chl) and Cr-spinel in porous zones (Fig. 11e-g). Actually, the nano-textures that have been characterized here with the TEM all converge towards epitaxial growth of secondary phases (oxides and silicates) upon spinel alteration.

The homogeneous spinel rim in zoned Cr-spinel from a dunite sample (sample O26; Trend 2) shows a perfect crystallographic continuity with the primary Cr-spinel core (Fig. 11). This homogeneous rim is enriched in Fe^{2+} and Cr^{3+} and contains little Fe^{3+} ($Fe^{3+}/Fe_{tot} < 0.18$). This compositional evolution is typical for high-temperature chlorite formation (Stage 1 described in Gervilla et al., 2012; Barra et al., 2014; Colás et al., 2019; Eslami et al., 2021; Roy et al., 2022). The rim is devoid of pores and inclusions although the chlorite-forming stage is believed to create porosity (Gervilla et al., 2012). Homogeneous core of zoned Cr-spinel has higher Cr# (0.63 – 0.73) and lower Mg# (0.42 – 0.49), compared to homogeneous rim (Cr#= 0.55 – 0.57; Mg#= 0.58 – 0.59; Table S6). At the nanoscale (Fig. S3), the transition from core to rim is smooth. Al and Cr diffusion at temperature below 700 °C is supposed to be ineffective, at least under dry condition as calculated with the diffusion data of Suzuki et al. (2008; Cr-Al interdiffusion coefficient < 10^{-29} m^2/s at temperature below 700°C). A dissolution - crystallization process is more likely with epitaxial growth of secondary spinel. Volume reduction is not accommodated by pores in homogeneous Cr-spinel rim. A second replacement process, Stage 2, involves the production of a network of nano to submicrometer-sized pores that are either empty or filled with secondary silicate products which, however, share crystallographic relationships with the host spinel matrix. In the porous zone, the pores seem to play a role in promoting the chemical exchange (e.g., Al and Mg removal, Fig. 10 section S3-A1) involved in Cr-spinel alteration. Chemical maps at the nanoscale highlight the role of the porosity for elemental transfer in and out the alteration zone. The presence of chlorite + serpentine + magnetite as reaction products indicates that partly altered textures, involving pores, form at serpentinization temperature, i.e., below 550 °C according to our thermochemical modeling. Again, Al diffusion is negligible at such low temperatures (Suzuki et al., 2008) and dissolution - recrystallization processes assisted by a porous network connects the alteration zone to the external silicate matrix (e.g., Putnis et al., 2005; Raufaste et al., 2011). Compared to the higher-temperature Stage 1, equilibration distances in Stage 2 are shorter and heterogeneity are preserved at the submicrometer scale (Fig. 10 and S3-A1). Reliable EPMA analyses of porous zones is difficult to obtain since the excitation volume is larger than chemical heterogeneity.

The development of porous zones is considered as the way to reach the ferrian Cr-spinel + magnetite stage which is not attained in the studied samples which are only slightly altered. Aqueous fluid was present in sufficient amount to achieve pervasive serpentinization of the host dunite. However, as outlined from the bulk rock dataset, the extent of fluid-rock interaction seems to have been somehow limited. Additional fluid rock interaction in shear zones where, in addition, spinel alteration can be promoted by deformation (*e.g.*, Kapsiotis, 2015; Satsukawa et al. 2015; Qiu and Zhu, 2018; Gervilla et al., 2019) is required to reach ferritchromite stage and ultimately magnetite ores. This is rather consistent with our field observation showing serpentinite-hosted magnetite ores occurred in a locus of fault system (Fig. 2c).

Concluding remarks

The following conclusions are drawn based on our observations, chemical and mineralogical measurements and mass balance calculations:

- Dry sub-solidus and early stages of Cr-spinel hydrothermal alteration are observed in chromitite pods from the Sabzevar ophiolite. The corresponding (primary) Cr-spinel in the chromitites and their dunite envelopes is subsequently altered under hydrothermal conditions. In other parts of the Sabzevar ophiolite, extensive fluid-rock interaction led to magnetite ore formation. Unexpectedly, Cr-spinel is thus a rather sensitive marker of fluid-rock interactions and their intensity.

- Plotted in a ternary Al-Cr-Fe^{3+} diagram, the composition of Cr-spinel from massive and semi-massive chromitites displays a trend (Trend 1) that differs from that of Cr-spinel in serpentinized dunite (Trend 2). Both alteration trends imply a progressive increase of Cr in Cr-spinel but it is associated with Fe^{3+} incorporation in serpentinized peridotites whereas in massive and semi-massive chromitites it is mainly related with the increase of Fe^{3+} along the alteration process. These two trends can be accounted for by a mass balance calculation considering different Cr-spinel/(Cr-spinel + silicate) ratios, involving a w/r = 1 and significant Mg solubility during hydrothermal alteration. The Cr-spinel/(Cr-spinel + silicate) ratio also controls spinel composition evolution during sub-solidus equilibration at temperature above 700 °C (e.g., Grieco et al., 2018).

-The early hydrothermal alteration texture is characterized by the formation of a partly altered Cr-spinel. Serpentine and chlorite filling pores developed during the serpentinization may have acted as pathways for reactive hydrothermal fluids. Porous texture development is rather restricted which might be related to limited fluid availability.

- Identical crystallographic orientation of lizardite/chlorite and Cr-spinel/magnetite reveals contemporaneous and topotactic formation of magnetite and phyllosilicates as hydrothermal alteration phases.

- Despite the expected very low-solubility of Cr-bearing spinel, changes in spinel composition upon mineral – fluid interactions at $T < 700°C$ are clearly possible and they imply isomorphic replacement at the nanoscale.

- The absence of significant iron exchange between the host (serpentinized) dunite and the chromitite pods is consistent with the lack of magnetite ore formation. In contrast, localities in the Sabzevar ophiolite belt where magnetite ores are present do show a significant mass transport of Fe and Al at a scale of a few tenths of meters with $w/r > 1000$.

- The present study at the mineral / rock scale did not elucidated the reasons for such differences in alteration extent which, in the frame of reaction – transport mediated by an aqueous fluid, may be related to differences in the efficiency of the hydrothermal fluid drainage or possible coupling with deformation in a system that is being exhumed.

Acknowledgments

This work was supported by a grant from Labex OSUG (Investissements d’avenir-ANR10 LABX56). We would like to express our sincere gratitude to University of Milan (Italy) for making polished thin sections. Valentina Batanova and Valérie Magnin are thanked for electron microprobe analyses conducted at the ISTerre (Grenoble). Nathaniel Findling is acknowledged for his help with Scanning Electron Microscopy. We are grateful to Kavandegan Bana Chromite Mining Development Company for logistical assistance during the fieldwork. We thank Nadia Malaspina for her editorial handling of our manuscript. Two anonymous reviewers are thanked for providing valuable constructive feedback and improvement suggestions on the research presented in this study.

References

Alikhani, M., Sohrabi Mehr, M., Mehrvarz, A., Akhoundi, H., Mehrvarz, A., Ansari, M., 2019. Geological Map of the Olang-Sir mine. KBC Exploration group, scale 1:25,000.

Arai, S., Miura, K., 2016. Formation and modification of chromitites in the mantle. Lithos 264, 277–295. https://doi.org/10.1016/j.lithos.2016.08.039

Arai, S., 2021. Genetic link between podiform chromitites in the mantle and stratiform chromitites in the crust: a hypothesis. Minerals 11(2), 209. https://doi.org/10.3390/min11020209

Ashley, P. M., 1975. Opaque mineral assemblage formed during serpentinization in the coolac ultramafic belt, New South Wales. Journal of the Geological Society of Australia 22(1), 91–102. https://doi.org/10.1080/00167617408728877

Augé, T., 1987. Chromite deposits in the northern Oman ophiolite: Mineralogical constraints. Mineralium Deposita 22(1), 1–10. https://doi.org/10.1007/BF00204235

Bahrudi, A., 1999. Geological Map of the Forumad Qadrangle: Tehran, Geological Survey of Iran, scale 1:100,000.

Bahrudi, A., Omrani, S.J., 1999. Geological Map of the Bashtin Qadrangle: Tehran, Geological Survey of Iran, scale 1:100,000.

Ballhaus, C., Berry, R. F., Green, D. H., 1991. High pressure experimental calibration of the olivine-orthopyroxene-spinel oxygen geobarometer: implications for the oxidation state of the upper mantle. Contributions to Mineralogy and Petrology *107*(1), 27–40. https://doi.org/10.1007/BF00311183

Barnes, S. J., 2000. Chromite in komatiites, II. Modification during greenschist to mid-amphibolite facies metamorphism. Journal of Petrology 41(3), 387–409. https://doi.org/10.1093/petrology/41.3.387

Barnes, S. J., Roeder, P. L., 2001. The range of spinel compositions in terrestrial mafic and ultramafic rocks. Journal of Petrology 42(12), 2279–2302. https://doi.org/10.1093/petrology/42.12.2279

Baroz, F., Macaudière, J., Montigny, R., Noghreyan, M., Ohnenstetter, M., Rocci, G., 1984. Ophiolites and Related Formations in the Central Part of the Sabzevar Range (Iran) and Possible Geotectonic Reconstructions. Neues Jahrbuch Für Geologie Und Paläontologie - Abhandlungen 168(2–3), 358–388. https://doi.org/10.1127/njgpa/168/1984/358

Barra, F., Gervilla, F., Hernández, E., Reich, M., Padrón-Navarta, J. A., González-Jiménez, J. M., 2014. Alteration patterns of chromian spinels from La Cabaña peridotite, south-central Chile. Mineralogy and Petrology 108(6), 819–836. https://doi.org/10.1007/s00710-014-0335-5

Batanova, V. G., Sobolev, A. V., Magnin, V., 2018. Trace element analysis by EPMA in geosciences: Detection limit, precision and accuracy. In IOP Conference Series: Materials Science and Engineering 304, p. 304(1)). https://doi.org/10.1088/1757-899X/304/1/012001

Beeson, M. H., Jackson, E. D., 1969. Chemical composition of altered chromites from the Stillwater Complex, Montana1. American Mineralogist 54(7–8), 1084–1100.

Bliss, N. W., MacLean, W. H., 1975. The paragenesis of zoned chromite from central Manitoba. Geochimica et Cosmochimica Acta 39(6–7), 973–990. https://doi.org/10.1016/0016-7037(75)90042-3

Borisova, A. Y., Ceuleneer, G., Kamenetsky, V. S., Arai, S., Béjina, F., Abily, B., Bindeman, I.N., Polvé, M., Parseval, P.D., Aigouy, T., Pokrovski, G. S., 2012. A new view on the petrogenesis of the Oman ophiolite chromitites from microanalyses of chromite-hosted inclusions. Journal of Petrology 53(12), 2411–2440. https://doi.org/10.1093/petrology/egs054

Burkhard, D. J. M., 1993. Accessory chromium spinels: Their coexistence and alteration in serpentinites. Geochimica et Cosmochimica Acta 57(6), 1297–1306. https://doi.org/10.1016/0016-7037(93)90066-6

Bussolesi, M., Grieco, G., Cavallo, A., Zaccarini, F., 2022. Different tectonic evolution of fast cooling ophiolite mantles recorded by olivine-spinel geothermometry: case studies from Iballe (Albania) and Nea Roda (Greece). Minerals 12, 64. https://doi.org/10.3390/min12010064.

Chichagov, A.V., Varlamov, D.A., Dilanyan, R.A., Dokina, T.N., Drozhzhina, N.A., Samokhvalova, O.L., Ushakovskaya, T.V., 2001. MINCRYST: A crystallographic database for minerals, local and network (WWW) versions. Crystallography Reports. 46, 876–879 (2001). https://doi.org/10.1134/1.140588

Colás, V., González-Jiménez, J. M., Griffin, W. L., Fanlo, I., Gervilla, F., O'Reilly, S. Y., … Proenza, J. A. (2014). Fingerprints of metamorphism in chromite: New insights from minor and trace elements. Chemical Geology 389, 137–152. https://doi.org/10.1016/j.chemgeo.2014.10.001

Colás, V., Padrón-Navarta, J. A., González-Jiménez, J. M., Fanlo, I., López Sánchez-Vizcaíno, V., Gervilla, F., Castroviejo, R., 2017. The role of silica in the hydrous metamorphism of chromite. Ore Geology Reviews 90, 274-286. https://doi.org/10.1016/j.oregeorev.2017.02.025

Colás, V., González-Jiménez, J.M., Camprubí, A., Proenza, J.A., Griffin, W.L., Fanlo, I., O'Reilly, S.Y., Gervilla, F., González-Partida, E., 2019. A reappraisal of the metamorphic history of the Tehuitzingo chromitite, Puebla state, Mexico. International Geology Reviews 61(14), 1706-1727. https://doi.org/10.1080/00206814.2018.1542633

Connolly, J. A. D., 2005. Computation of phase equilibria by linear programming: A tool for geodynamic modeling and its application to subduction zone decarbonation. Earth and Planetary Science Letters 236(1–2), 524–541. https://doi.org/10.1016/j.epsl.2005.04.033

Coogan, L. A., Saunders, A. D., Wilson, R. N., 2014. Aluminum-in-olivine thermometry of primitive basalts: Evidence of an anomalously hot mantle source for large igneous provinces. Chemical Geology 368, 1–10. https://doi.org/10.1016/j.chemgeo.2014.01.004

Engi, M., 1984. Equilibria involving Al-Cr spinel; Mg-Fe exchange with olivine; experiments, thermodynamic analysis, and consequences for geothermometry; erratum. American Journal of Science 284(3), 288. https://doi.org/10.2475/ajs.284.3.288

Eslami, A., Malvoisin, B., Brunet, F., Kananian, A., Bach, W., Grieco, G., Cavallo, A., Gatta, G. D., 2021. Podiform magnetite ore(s) in the Sabzevar ophiolite (NE Iran): oceanic hydrothermal alteration of a chromite deposit. Contributions to Mineralogy and Petrology 176(43). https://doi.org/10.1007/s00410-021-01799-0

Evans, B. W., Frost, B. R., 1975. Chrome spinel in progressive metamorphism—a preliminary analysis. Geochimica et Cosmochimica Acta 39, 959–972.

Faramarzi, R., Alikhani, M., Pourfaraj, H., Akhoundi, H., Mehrvarz, A., Sohrabi Mehr, M., Ansari, M., 2017. Geological Map of the Cheshmeh-Khan, KBC Exploration group, scale 1:25,000.

Faramarzi, R., Pourfaraj, H., Alikhani, M., Akhoundi, H., Mehrvarz, A., Sohrabi Mehr, M., Ansari, M., 2018. Geological Map of the Cheshmeh-Palangan, KBC Exploration group, scale 1:25,000.

Fleet, M. E., Angeli, N., Yuanming Pan., 1993. Oriented chlorite lamellae in chromite from the Pedra Branca mafic- ultramafic complex, Ceara, Brazil. American Mineralogist 78(1–2), 68–74.

Gervilla, F., Padrón-Navarta, J. A., Kerestedjian, T., Sergeeva, I., González-Jiménez, J. M., Fanlo, I., 2012. Formation of ferrian chromite in podiform chromitites from the Golyamo Kamenyane serpentinite, Eastern Rhodopes, SE Bulgaria: A two-stage process. Contributions to Mineralogy and Petrology 164(4), 643–657. https://doi.org/10.1007/s00410-012-0763-3

Gervilla, F., Asta, M. P., Fanlo, I., Grolimund, D., Ferreira-Sánchez, D., Samson, V. A., … Sergeeva, I., 2019. Diffusion pathways of Fe^{2+} and Fe^{3+} during the formation of ferrian chromite:

a µXANES study. Contributions to Mineralogy and Petrology 174(8). https://doi.org/10.1007/s00410-019-1605-3

González-Jiménez, J. M., Griffin, W. L., Proenza, J. A., Gervilla, F., O'Reilly, S. Y., Akbulut, M., Pearson, N.J., Arai, S., 2014. Chromitites in ophiolites: How, where, when, why? Part II. The crystallization of chromitites. Lithos 189, 140-158. https://doi.org/10.1016/j.lithos.2013.09.008

González-Jiménez, J. M., Kerestedjian, T., Proenza, J. A., Gervilla, F., 2009. Metamorphism on chromite ores from the Dobromirtsi Ultramafic Massif, Rhodope Mountains (SE Bulgaria). Geologica Acta 7(4), 413–429. https://doi.org/10.1344/104.000001447

Greenbaum, D., 1977. The chromitiferous rocks of the Troodos ophiolite complex, Cyprus. Economic Geology 72(7), 1175–1194. https://doi.org/10.2113/gsecongeo.72.7.1175

Grieco, G., Bussolesi, M., Tzamos, E., Rassios, A. E., Kapsiotis, A., 2018. Processes of primary and re-equilibration mineralization affecting chromitite ore geochemistry within the Vourinos ultramafic sequence, Vourinos ophiolite (West Macedonia, Greece). Ore Geology Reviews 95, 537-551. https://doi.org/10.1016/j.oregeorev.2018.03.009

Gauthier, M., Corrivaux, L., Trottier, L. J., Cabri, J., Laflamme, J. H. G., Bergeron, M., 1990. Chromitites platinifères des complexes ophiolitiques de l'Estrie-Beauce, Appalaches du sud du Québec. Mineralium Deposita 25(3), 169–178. https://doi.org/10.1007/BF00190378

Grieco, G., Merlini, A., 2012. Chromite alteration processes within Vourinos ophiolite. International Journal of Earth Sciences 101(6), 1523–1533. https://doi.org/10.1007/s00531-011-0693-8

Haslam, H. W., Harding, R. R., Tresham, A. E., 1976. Chromite-chlorite intergrowths in peridotite at Chimwadzulu Hill, Malawi. Mineralogical Magazine 40(315), 695–701. https://doi.org/10.1180/minmag.1976.040.315.03

Kapsiotis, A. N., 2015. Alteration of chromitites from the Voidolakkos and Xerolivado mines, Vourinos ophiolite complex, Greece: Implications for deformation-induced metamorphism. Geological Journal 50(6), 739–763. https://doi.org/10.1002/gj.2590

Kazemi, Z., Ghasemi, H., Tilhac, R., Griffin, W., Moghadam, H. S., O'Reilly, S., Mousivand, F., 2019. Late cretaceous subduction-related magmatism on the southern edge of Sabzevar basin, NE Iran. Journal of the Geological Society 176(3), 530–552. https://doi.org/10.1144/jgs2018-076

Khalil, I., El-Makky, A. M., 2009. Alteration mechanisms of chromian-spinel during serpentinization at wadi sifein area, eastern desert, Egypt. Resource Geology 59(2), 194–211. https://doi.org/10.1111/j.1751-3928.2009.00090.x

Lensch, G., Davoudzadeh, M., 1982. Ophiolites in Iran. Neues Jahrbuch für Geologie und Paläontologie– Monatshefte 5, 306–20.

Lensch, G., 1980. Major element geochemistry of the ophiolites in north-eastern Iran. In: Panayiotou, A. (Ed.). Proceedings to International Ophiolite Symposium. Ministry of Agriculture and Natural Resources, Geological Survey Department, Republic of Cyprus, pp.389-401.

Lorand, J. P., Ceuleneer, G., 1989. Silicate and base-metal sulfide inclusions in chromites from the Maqsad area (Oman ophiolite, Gulf of Oman): A model for entrapment. Lithos 22(3), 173–190. https://doi.org/10.1016/0024-4937(89)90054-6

Malvoisin, B., Zhang, C., Müntener, O., Baumgartner, L. P., & Kelemen, P. B. (2020). Measurement of volume change and mass transfer during serpentinization: Insights from the oman drilling project. *Journal of Geophysical Research*, 125(5).

Mellini, M., Rumori, C., Viti, C., 2005. Hydrothermally reset magmatic spinels in retrograde serpentinites: Formation of “ferritchromit” rims and chlorite aureoles. Contributions to Mineralogy and Petrology 149(3), 266–275. https://doi.org/10.1007/s00410-005-0654-y

Mitra, S., Pal, T., Maity, P.K., Moon, H-S., 1992. Ferritchromite and its opto-chemical behaviour. Minralogical Journal 16 (4), 173-186.

Mukherjee, R., Mondal, S. K., Rosing, M. T., Frei, R. 2010. Compositional variations in the Mesoarchean chromites of the Nuggihalli schist belt, Western Dharwar Craton (India): Potential parental melts and implications for tectonic setting. Contributions to Mineralogy and Petrology 160(6), 865–885. https://doi.org/10.1007/s00410-010-0511-5

Noghreyan, M., 1982. Evolution geochimique, mineralogique et structurale d’un edificeophiolitique singulier: le massif de Sabzevar (partie centrale), NE de l’Iran. TheseDoc. d’Etat, Universite de Nancy, France, p 239

Onyeagocha, A. C., 1974. Alteration of Chromite from the Twin Sisters Dunite, Washington. American Mineralogist 59(5–6), 608–612.

Oze, C., Fendorf, S., Bird, D. K., Coleman, R. G., 2004. Chromium geochemistry in serpentinized ultramafic rocks and serpentine soils from the Franciscan complex of California. American Journal of Science 304(1), 67–101. https://doi.org/10.2475/ajs.304.1.67

Pinsent, R. H., Hirst, D. M., 1977. The metamorphism of the blue river ultramafic body, cassiar, British Columbia, Canada. Journal of Petrology 18(4), 567–594. https://doi.org/10.1093/petrology/18.4.567

Prabhakar, N., Bhattacharya, A., 2013. Origin of zoned spinel by coupled dissolution-precipitation and inter-crystalline diffusion: Evidence from serpentinized wehrlite, Bangriposi, Eastern India. Contributions to Mineralogy and Petrology 166(4), 1047–1066. https://doi.org/10.1007/s00410-013-0909-y

Putnis, C. V., Tsukamoto, K., Nishimura, Y., 2005. Direct observations of pseudomorphism: Compositional and textural evolution at a fluid-solid interface. American Mineralogist 90(11–12), 1909–1912. https://doi.org/10.2138/am.2005.1990

Qiu, T., Zhu, Y., 2018. Chromian spinels in highly altered ultramafic rocks from the Sartohay ophiolitic mélange, Xinjiang, NW China. Journal of Asian Earth Sciences 159, 155–184. https://doi.org/10.1016/j.jseaes.2017.08.011

Radfar, J., Kohansal, R., 2001. Geological Map of the Davarzan Qadrangle: Tehran, Geological Survey of Iran, scale 1:100,000.

Rahmani, F., Mackizadeh, M. A., Noghreyan, M., Marchesi, C., Garrido, C. J., 2020. Petrology and geochemistry of mafic and ultramafic cumulate rocks from the eastern part of the Sabzevar ophiolite (NE Iran): Implications for their petrogenesis and tectonic setting. Geoscience Frontiers 11(6), 2347–2364. https://doi.org/10.1016/j.gsf.2020.02.004

Rahmati Ilkhchi, M., 1999. Geological Map of the Joghatay Qadrangle: Tehran, Geological Survey of Iran, scale 1:100,000.

Rassios, A., Kostopoulos, D., 1990. The geochemistry of dunite and its relation to the position of chromitites in the Vourinos ophiolite complex, Greece, In: Malpas, J., Moores, E., Panayiotou, A. and Xenophontos, C., eds, Ophiolites, Oceanic Crustal Analogues. Proc. Symp. "Troodos 1987", Nicosia, Cyprus, 593-604.

Raufaste, C., Jamtveit, B., John, T., Meakin, P., Dysthe, D. K., 2011. The mechanism of porosity formation during solvent-mediated phase transformations. Proceedings of the Royal Society A: Mathematical, Physical and Engineering Sciences 467(2129), 1408–1426. https://doi.org/10.1098/rspa.2010.0469

Rauch, E. F., Véron, M., 2014. Automated crystal orientation and phase mapping in TEM. Materials Characterization 98, 1-9. https://doi.org/10.1016/j.matchar.2014.08.010

Rossetti, F., Nasrabady, M., Vignaroli, G., Theye, T., Gerdes, A., Razavi, M. H., Vaziri, H. M., 2010. Early Cretaceous migmatitic mafic granulites from the Sabzevar range (NE Iran):

Implications for the closure of the Mesozoic peri-Tethyan oceans in central Iran. Terra Nova 22(1), 26–34. https://doi.org/10.1111/j.1365-3121.2009.00912.x

Roy, S., Bandyopadhyay, D., Morishita, T., Dhar, A., Koley, M., Chattopadhaya, S., Karmakar, A., Gosh, B., 2022. Microtextural evolution of chrome spinels in dunites from Mayodia ophiolite complex, Arunachal Pradesh, India: implications for a missing link in the “two-stage” alteration mechanism. Lithos 420-421, 106719. https://doi.org/10.1016/j.lithos.2022.106719

Sack, R. O., Ghiorso, M. S., 1991. Chromian spinels as petrogenetic indicators: thermodynamics and petrological applications. American Mineralogist 76(5–6), 827–847.

Satsukawa, T., Piazolo, S., González-Jiménez, J. M., Colás, V., Griffin, W. L., O’Reilly, S. Y., … Kerestedjian, T. N., 2015. Fluid-present deformation aids chemical modification of chromite: Insights from chromites from Golyamo Kamenyane, SE Bulgaria. Lithos 228–229, 78–89. https://doi.org/10.1016/j.lithos.2015.04.020

Shafaii Moghadam, H., Zaki Khedr, M., Arai, S., Stern, R. J., Ghorbani, G., Tamura, A., & Ottley, C. J., 2015. Arc-related harzburgite-dunite-chromitite complexes in the mantle section of the Sabzevar ophiolite, Iran: A model for formation of podiform chromitites. Gondwana Research 27(2), 575–593. https://doi.org/10.1016/j.gr.2013.09.007

Shafaii Moghadam, H., Corfu, F., Chiaradia, M., Stern, R. J., Ghorbani, G., 2014. Sabzevar Ophiolite, NE Iran: Progress from embryonic oceanic lithosphere into magmatic arc constrained by new isotopic and geochemical data. Lithos 210–211, 224–241. https://doi.org/10.1016/j.lithos.2014.10.004

Shafaii Moghadam, H., Stern, R. J., 2015. Ophiolites of Iran: Keys to understanding the tectonic evolution of SW Asia: (II) Mesozoic ophiolites. Journal of Asian Earth Sciences 100, 31-59. https://doi.org/10.1016/j.jseaes.2014.12.016

Shen, P., Hwang, S.-L., Chu, H.-T., Jeng, R.-C., 1988. STEM study of “ferritchromit” from the Heng-Chun chromitite. American Mineralogist 73 (3-4), 383–388.

Shojaat, B., Hassanipak, A. A., Mobasher, K., Ghazi, A. M., 2003. Petrology, geochemistry and tectonics of the Sabzevar ophiolite, North Central Iran. Journal of Asian Earth Sciences 21, 1053–1067. https://doi.org/10.1016/S1367-9120(02)00143-8

Sobolev, A. V, Hofmann, A. W., Kuzmin, D. V, Yaxley, G. M., Arndt, N. T., Chung, S.-L., Danyushevsky, L.V., Elliott, T., Frey, F.A., Garcia, M.O., Gurenko, A.A., Kamenetsky, V.S., Kerr, A.C., Krivolutskaya, N.A., Matvienkov, V.V., Nikogosian, I.K., Rocholl, A., Sigurdsson, I.A., Sushchevskaya, N.M., Teklay, M., 2007. The amount of recycled crust in sources of mantle-derived melts. Science 316(5823), 412–417. https://doi.org/10.1126/science.1138113.

Soleimani, M., Shokri, B.J., 2016. Intrinsic geological model generation for chromite pods in the Sabzevar ophiolite complex, NE Iran. Ore Geology Reviews, 78, 138-150.

Spangenberg, K., 1943. Die chromitlaagerstatte von tampedal in Zobten. Z Prakt Geol 51, 13–35.

Suzuki, A. M., Yasuda, A., Ozawa, K., 2008. Cr and Al diffusion in chromite spinel: Experimental determination and its implication for diffusion creep. Physics and Chemistry of Minerals 35(8), 433–445. https://doi.org/10.1007/s00269-008-0238-2.

Sverjensky, D. A., Harrison, B., Azzolini, D., 2014. Water in the deep Earth: The dielectric constant and the solubilities of quartz and corundum to 60kb and 1200°C. Geochimica et Cosmochimica Acta 129, 125–145. https://doi.org/10.1016/j.gca.2013.12.019

Ulmer, G. C., 1974. Alteration of chromite during serpentinization in the Pennsylvania-Maryland District. American Mineralogist 59(1969), 1236–1241.

Wylie, A. G., Candela, P. A., Burke, T. M., 1987. Compositional zoning in unusual Zn-rich chromite from the Sykesville district of Maryland and its bearing on the origin of “ferritchromite”. American Mineralogist 72(3–4), 413–422.

Figure Captions

Fig. 1. (a) Outline map showing the distribution of Mesozoic ophiolites in Iran; (b) Simplified geological map of the Sabzevar ophiolite belt (modified after Shafaii Moghadam et al. 2014); (c) Simplified geological map of the study area in the central sector of Sabzevar ophiolite belt modified from the 1:100,000 geological quadrangle maps of Forumad (Bahrudi, 1999), Joghatay (Rahmati Ilkhchi, 1999), Bashtin (Bahrudi and Omrani, 1999) and Davarzan (Radfar and Kohansal, 2001). Detailed geological maps with the study areas marked with black rectangles are shown in Figure 2.

Fig. 2. Geological maps of the Kuh Siah (a) and Olang Sir (b) areas modified from the 1:25,000 geological maps of Cheshmeh Khan (Faramarzi et al., 2017) and Chesmeh Palangan (Faramarzi et al., 2018) and Olang Sir (Alikhani et al., 2019). Location of the studied chromitite deposits are shown with white-filled circles.

Fig. 3. Field photographs showing the different chromitite textures in the Sabzevar ophiolite. (a) Deformed massive chromitite pod. Note the contact between harzburgite and chromitite/dunite is tectonic. (b) Nodular chromitite embedded dunite; (c) magnetite ore vein hosted by serpentinized dunite (sample O1).

Fig. 4. Backscattered-electron images of partly altered (a-d) and zoned Cr-spinels (e-i) in the Sabzevar ophiolite. (a) Heterogeneous ferrian Cr-spinel (Fe-Cr-Spl) domains around homogenous Cr-spinel (Cr-Spl) (sample EB-4). (b) Heterogeneous ferrian Cr-spinel (Fe-Cr-Spl) along the cracks and boundaries of homogeneous Cr-spinel (Cr-Spl) (sample O27). (c) Porous ferrian Cr-

spinel (Fe-Cr-Spl) with serpentine and chlorite inclusions at marginal parts of homogeneous Cr-spinel core (sample IM-1b); (d) Magnetite (Mgt) veinlets rumbling through the homogeneous Cr-spinel (sample SI-2c).

Fig 5. Backscattered-electron images of dunite samples: (a) magnetite (Mgt) cut through the mesh textured serpentine (Srp) mixed at the submicrometer scale with brucite (Brc); (b) subhedral chromite (Chr) grain with ferrian chromite (Fe-Chr) alteration at the rim. (c-d) zoned Cr-spinel with homogeneous Cr-spinel core (Cr-Spl) surrounded by homogeneous ferrian Cr-spinel rim (Fe-Cr-Spl) (sample O26). (e) Sharp contact between homogeneous Cr-spinels. (f) Porous Cr-spinel with tiny globular silicate inclusions; (g) Porous Cr-spinel with sheet silicate inclusions; Blue lines indicate the location TEM lamella.

Fig. 6. Compositional plot of chromitites (a) and spinels (b) on a ternary diagram Cr-Al-Fe^{3+} showing two distinct compositional trends (c), total iron (apfu on a 4 oxygen basis) (d) and Mg# variations through alteration processes.

Fig. 7. Compositional variations of Cr-spinel grains from the Sabzevar ophiolite, in terms of Cr#, Mg#, Fe+/(Fe^{3+} + Fe^{2+}) and NiO (wt. %). Fields for the Sabzevar magnetite ore (blue dashed line) and its host dunite (red dashed line) are given for comparison (Eslami et al., 2021).

Fig. 8. Bulk rock composition (in oxide weight percent) of chromitites, magnetitites and associated serpentinized dunites from Sabzevar ophiolite. (a) SiO_2-Cr_2O_3-Fe_2O_3tot ternary diagram. The color of the symbols corresponds to the Al_2O_3 content. Composition of chromitites and associated serpentinized dunite envelopes is displayed with diamonds. Composition of magnetitites and associated serpentinized dunite envelopes are displayed with circles. (b) Al_2O_3 – Cr_2O_3 diagram. Dashed lines are calculated considering a Cr-spinel with a Al_2O_3/Cr_2O_3 ratio of 0.53 deduced from EMPA on spinel cores. (c) Fe_2O_3 – Cr_2O_3 diagram. Colored lines are calculated compositional trends assuming isochemical hydration of a bimineralic dunite (serpentinization) composed of olivine with Mg# = 0.922 (blue line) and 0.938 (red line) and Cr-spinel with a Al_2O_3/Cr_2O_3 mass ratio of 0.65 as deduced from EPMA.

Fig. 9. Cr (ppm) versus Zn (a), Co (b) and V contents (c) in chromitites and associated serpentinized dunites in the Sabzevar ophiolite.

Fig. 10. Bright Field Image and EDS-STEM element maps of the porous Fe-Cr-spinel/homogeneous Cr-spinel and porous Fe-Cr-spinel /homogeneous Fe-Cr-spinel. Abbreviation: Srp (serpentine), Mgt (magnetite), Cr-spl (Cr-spinel), Liz (Lizardite).

Fig. 11. Orientation maps (a-d) of spinels and associated silicate inclusions in the same region as Fig. 4 (a: S2-A1; b: S2-A2; c: S3-A2 and d: S3-A1). (e-f) Colour-coded inverse pole figures used for displaying Cr-spinel/magnetite (e) and lizardite (f) orientation in (a-d). (g) pole figures of lizardite and spinels in (a-d).

Fig. 12. Evolution of spinel composition in the mass balance model. The stars represent the initial spinel composition which evolves during chlorite and serpentine formation. The color corresponds to the Mg/(Mg + Fe^{2+}) ratio in spinel. (a) model results for water to rock ratio of 0.01, 1, 5 and 10. X_{Chr} = 0.1 and X_{Ol} = 1. (b): model results for XChr of 0.01, 0.3, 0.5 and 0.7. X_{Ol} = 1 and the water to rock ratio is fixed to 5.

Table Captions:

Table 1. Dunite mineral modes (wt.%) and X_{Mg} of olivine were retrieved from least-square (LSQ) regression through the bulk dunite composition

Table 2. Chromitite mineral modes (wt.%) retrieved from LSQ regression through the chromitite bulk rock composition

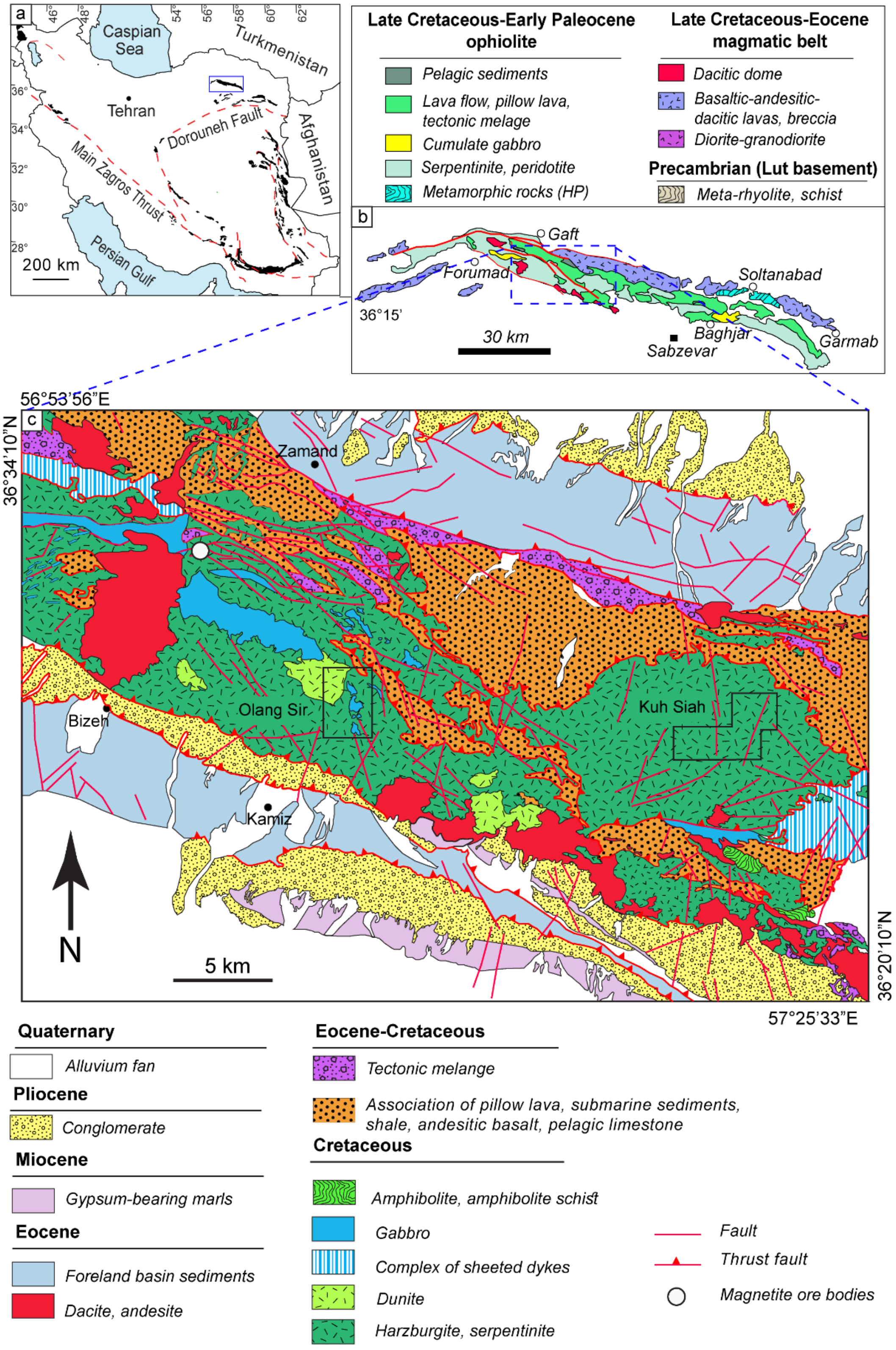
a
46°
48°
54°
56°
58°
60°
62°
36°
34°
32°
30°
28°
Caspian Sea
Turkmenistan
Tehran
Dorouneh Fault
Afghanistan
Main Zagros Thrust
Persian Gulf
200 km
Late Cretaceous-Early Paleocene ophiolite
Pelagic sediments
Lava flow, pillow lava, tectonic melage
Cumulate gabbro
Serpentinite, peridotite
Metamorphic rocks (HP)
Late Cretaceous-Eocene magmatic belt
Dacitic dome
Basaltic-andesitic-dacitic lavas, breccia
Diorite-granodiorite
Precambrian (Lut basement)
Meta-rhyolite, schist
b
Gaft
Forumad
Soltanabad
36°15'
30 km
Baghjar
Sabzevar
Garmab
56°53'56"E
c
36°34'10"N
Zamand
Olang Sir
Kuh Siah
Bizeh
Kamiz
N
5 km
36°20'10"N
57°25'33"E
Quaternary
Alluvium fan
Pliocene
Conglomerate
Miocene
Gypsum-bearing marls
Eocene
Foreland basin sediments
Dacite, andesite
Eocene-Cretaceous
Tectonic melange
Association of pillow lava, submarine sediments, shale, andesitic basalt, pelagic limestone
Cretaceous
Amphibolite, amphibolite schist
Gabbro
Complex of sheeted dykes
Dunite
Harzburgite, serpentinite
Fault
Thrust fault
Magnetite ore bodies

Fig. 1

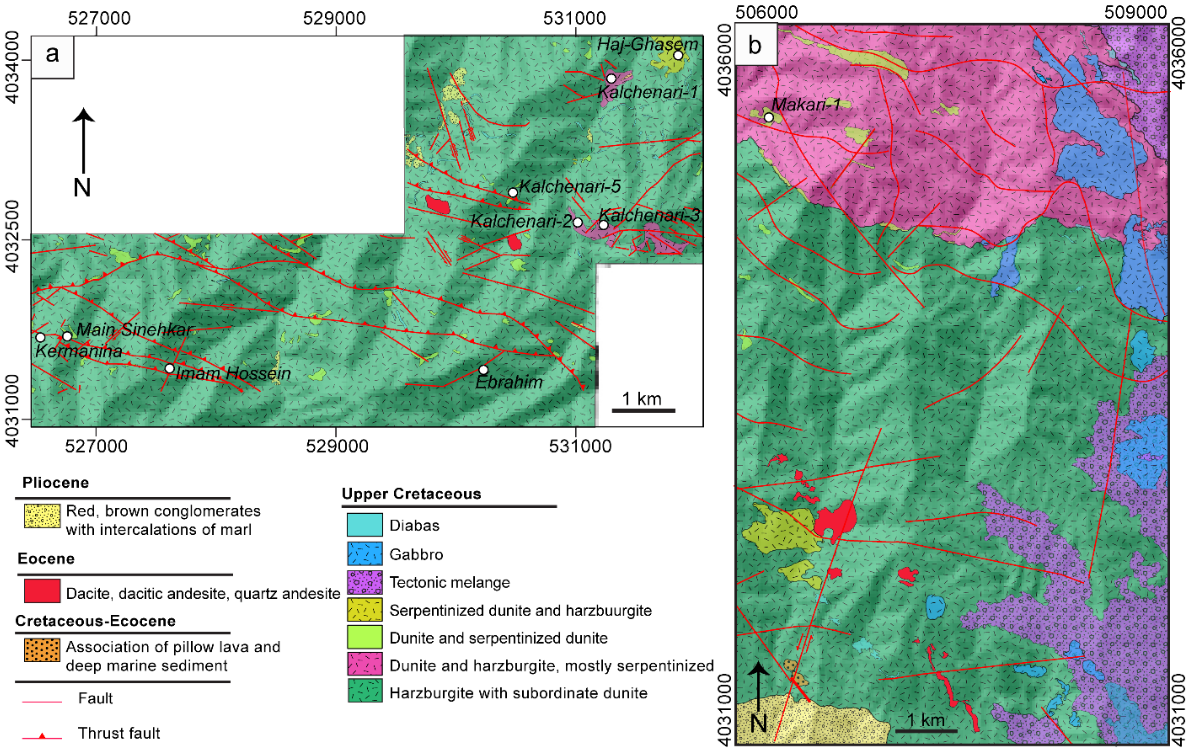
a
527000
529000
531000
4034000
4032500
4031000
N
Haj-Ghasem
Kalchenari-1
Kalchenari-5
Kalchenari-2
Kalchenari-3
Main Sinehkar
Kermanina
Imam Hossein
Ebrahim
1 km
b
506000
509000
4036000
4031000
Makari-1
N
1 km
Pliocene
Red, brown conglomerates with intercalations of marl
Eocene
Dacite, dacitic andesite, quartz andesite
Cretaceous-Ecocene
Association of pillow lava and deep marine sediment
Fault
Thrust fault
Upper Cretaceous
Diabas
Gabbro
Tectonic melange
Serpentinized dunite and harzbuurgite
Dunite and serpentinized dunite
Dunite and harzburgite, mostly serpentinized
Harzburgite with subordinate dunite

Fig. 2.

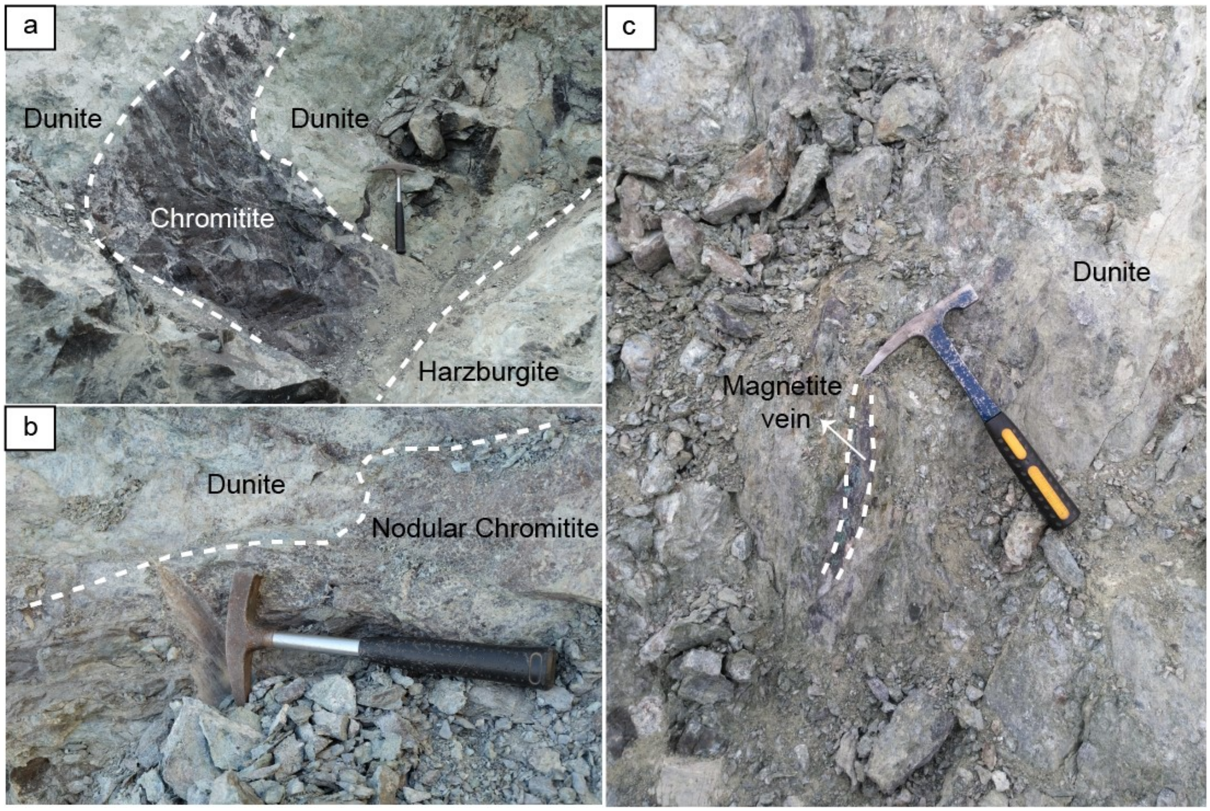
a
Dunite
Dunite
Chromitite
Harzburgite
b
Dunite
Nodular Chromitite
c
Dunite
Magnetite vein

Fig. 3.

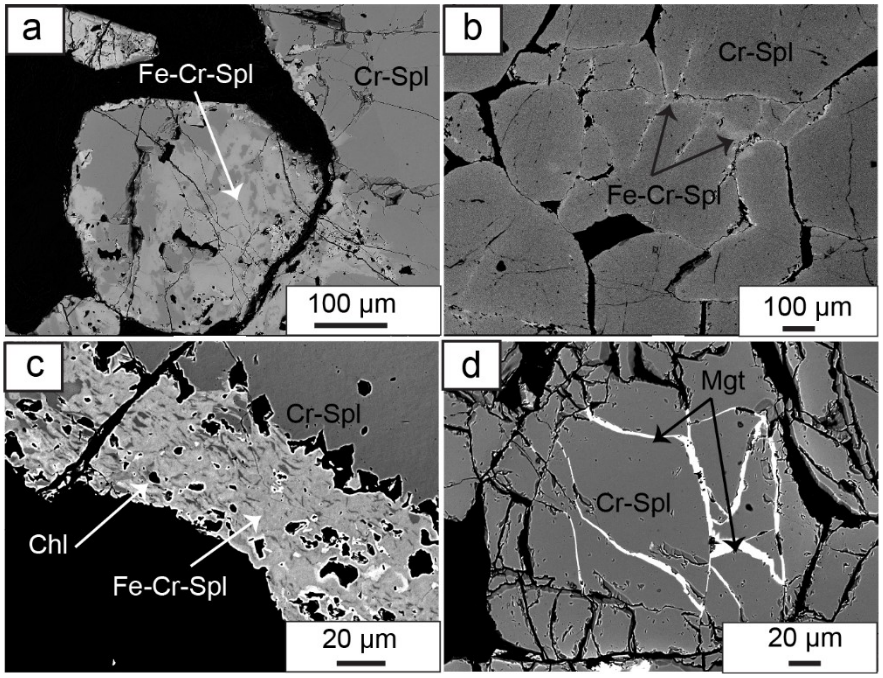
a
Fe-Cr-Spl
Cr-Spl
100 μm
b
Cr-Spl
Fe-Cr-Spl
100 μm
c
Cr-Spl
Chl
Fe-Cr-Spl
20 μm
d
Mgt
Cr-Spl
20 μm

Fig. 4.

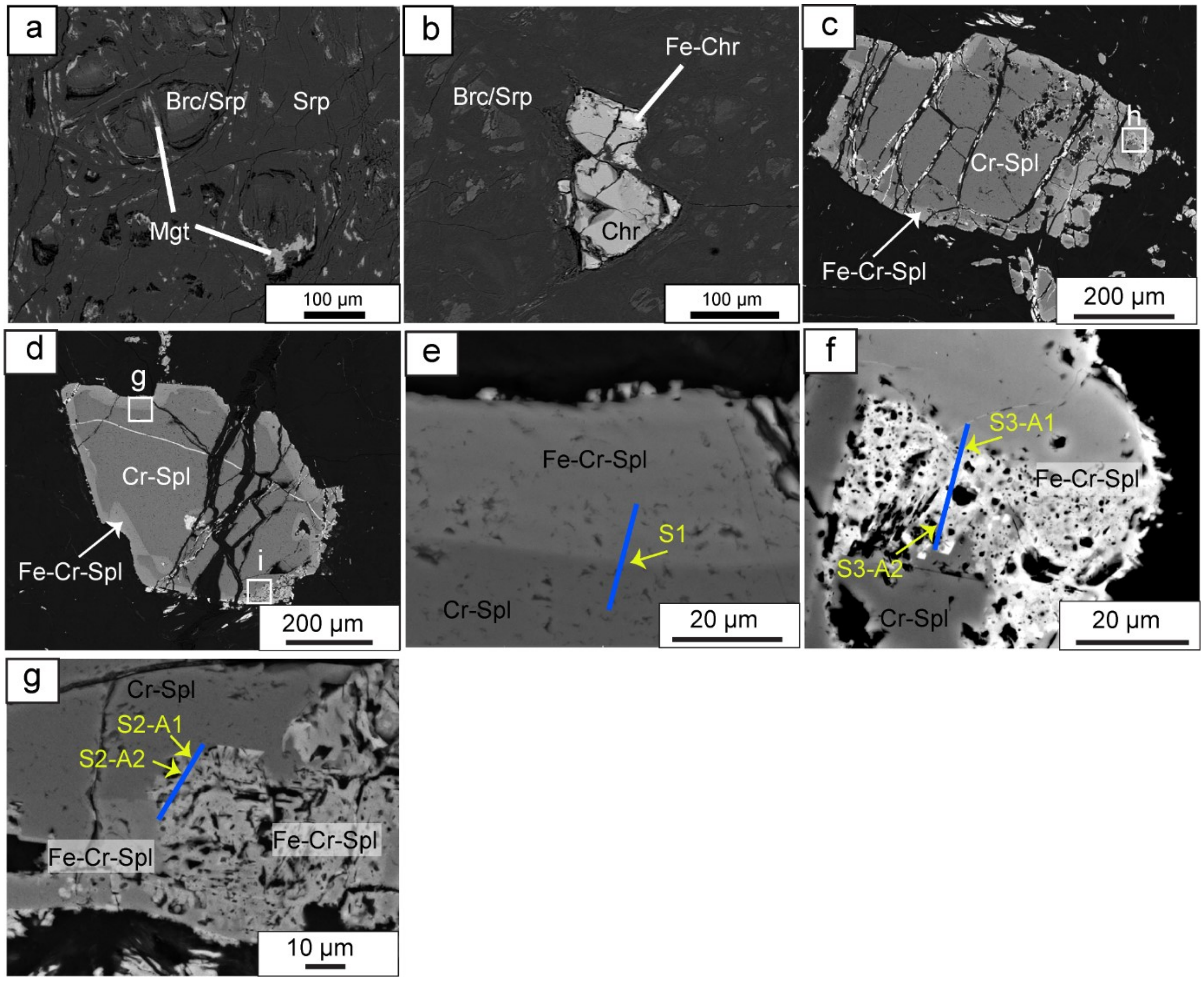

1084

1085 **Fig. 5.**

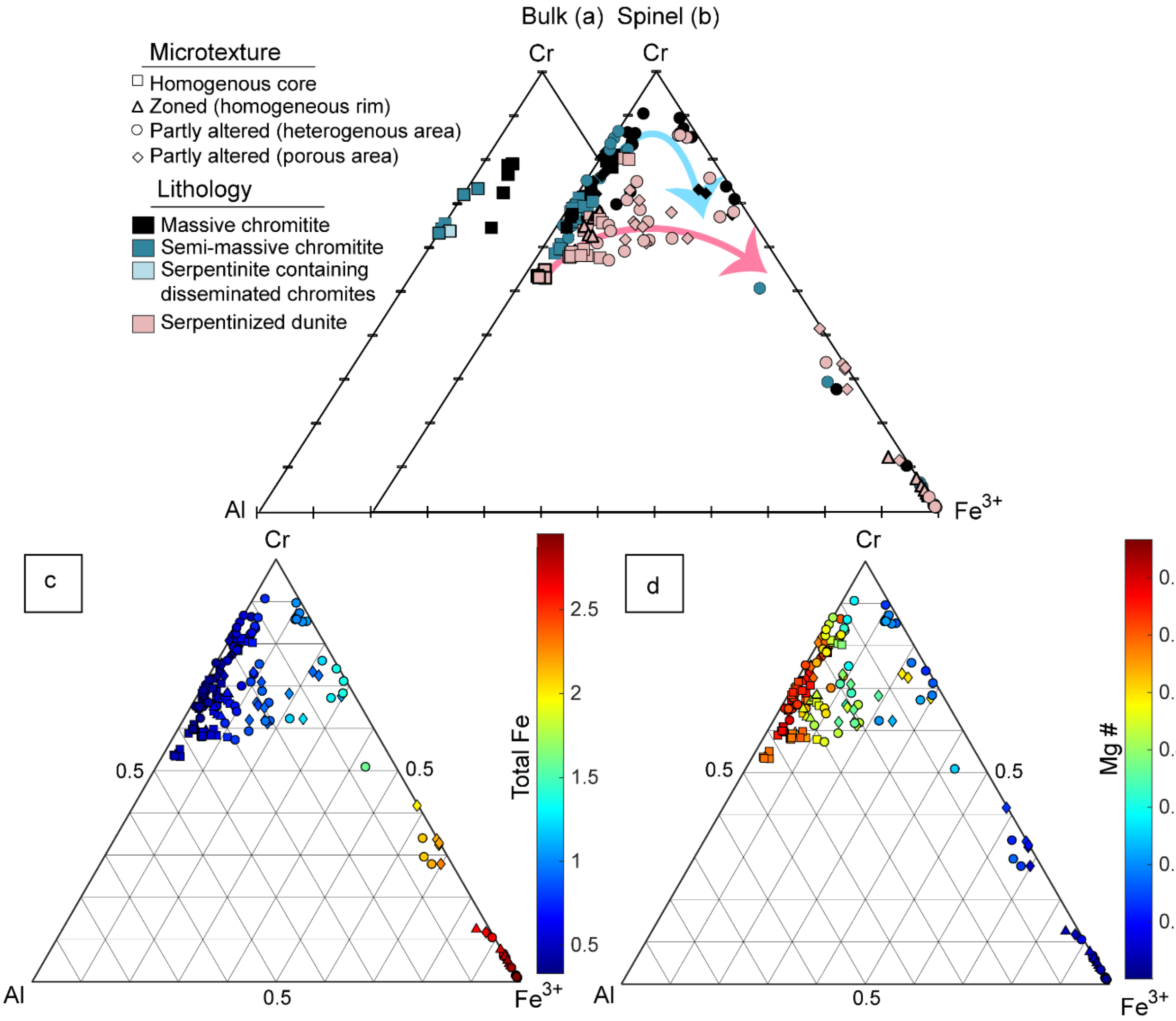
Bulk (a) Spinel (b)
Cr
Cr
Microtexture
□ Homogenous core
Δ Zoned (homogeneous rim)
○ Partly altered (heterogenous area)
◇ Partly altered (porous area)
Lithology
Massive chromitite
Semi-massive chromitite
Serpentinite containing disseminated chromites
Serpentinized dunite
Al
Fe^{3+}
c
Cr
0.5
0.5
Al
0.5
Fe^{3+}
Total Fe
2.5
2
1.5
1
0.5
d
Cr
0.5
0.5
Al
0.5
Fe^{3+}
Mg #
0.7
0.6
0.5
0.4
0.3
0.2
0.1

Fig. 6.

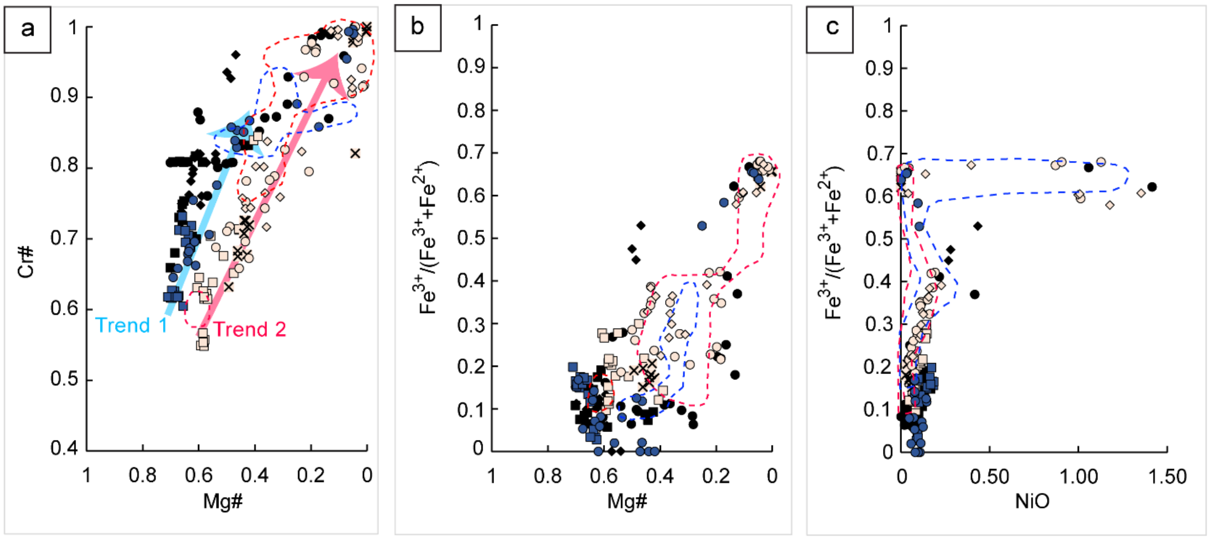
a
Cr#
1
0.9
0.8
0.7
0.6
0.5
0.4
Trend 1
Trend 2
1
0.8
0.6
0.4
0.2
0
Mg#
b
$Fe^{3+}/(Fe^{3+}+Fe^{2+})$
1
0.9
0.8
0.7
0.6
0.5
0.4
0.3
0.2
0.1
0
1
0.8
0.6
0.4
0.2
0
Mg#
c
$Fe^{3+}/(Fe^{3+}+Fe^{2+})$
1
0.9
0.8
0.7
0.6
0.5
0.4
0.3
0.2
0.1
0
0
0.50
1.00
1.50
NiO

Fig. 7.

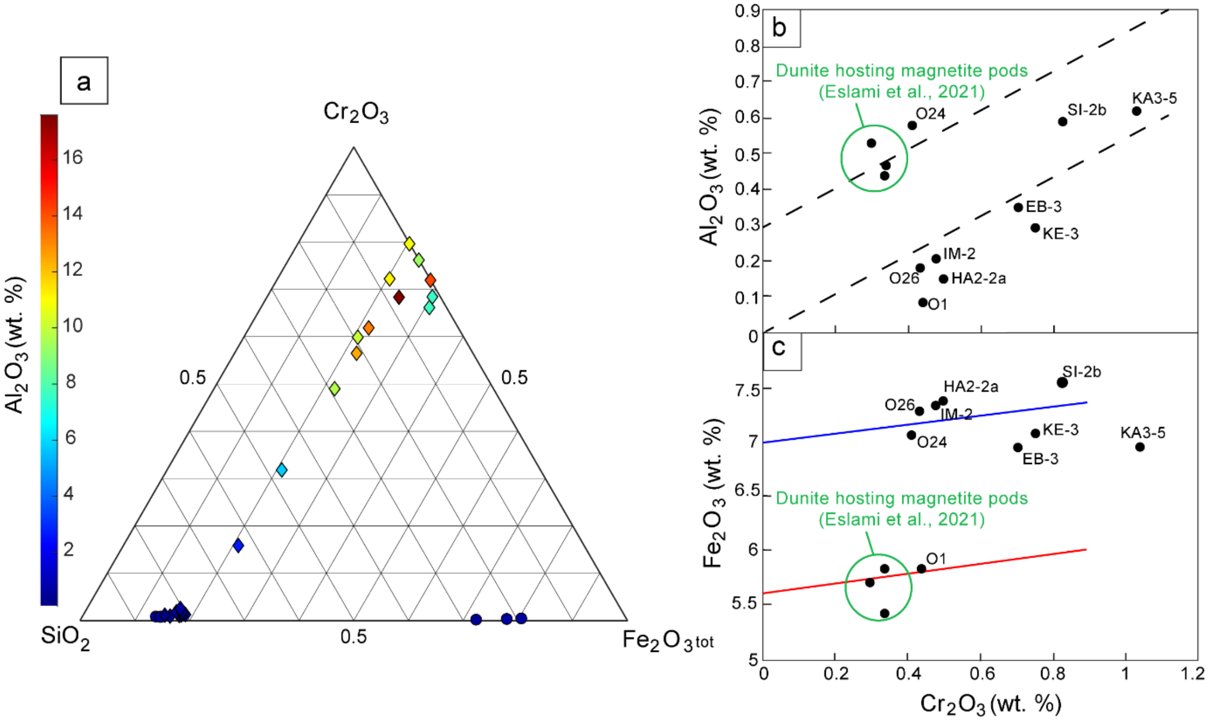
a
Cr$_2$O$_3$
Al$_2$O$_3$ (wt. %)
16
14
12
10
8
6
4
2
0.5
0.5
SiO$_2$
0.5
Fe$_2$O$_3$ tot
b
0.9
0.8
0.7
0.6
0.5
0.4
0.3
0.2
0.1
0
Al$_2$O$_3$ (wt. %)
Dunite hosting magnetite pods
(Eslami et al., 2021)
O24
SI-2b
KA3-5
EB-3
KE-3
IM-2
O26
HA2-2a
O1
c
7.5
7
6.5
6
5.5
5
Fe$_2$O$_3$ (wt. %)
SI-2b
HA2-2a
O26
IM-2
KE-3
KA3-5
O24
EB-3
Dunite hosting magnetite pods
(Eslami et al., 2021)
O1
0
0.2
0.4
0.6
0.8
1
1.2
Cr$_2$O$_3$ (wt. %)

Fig. 8.

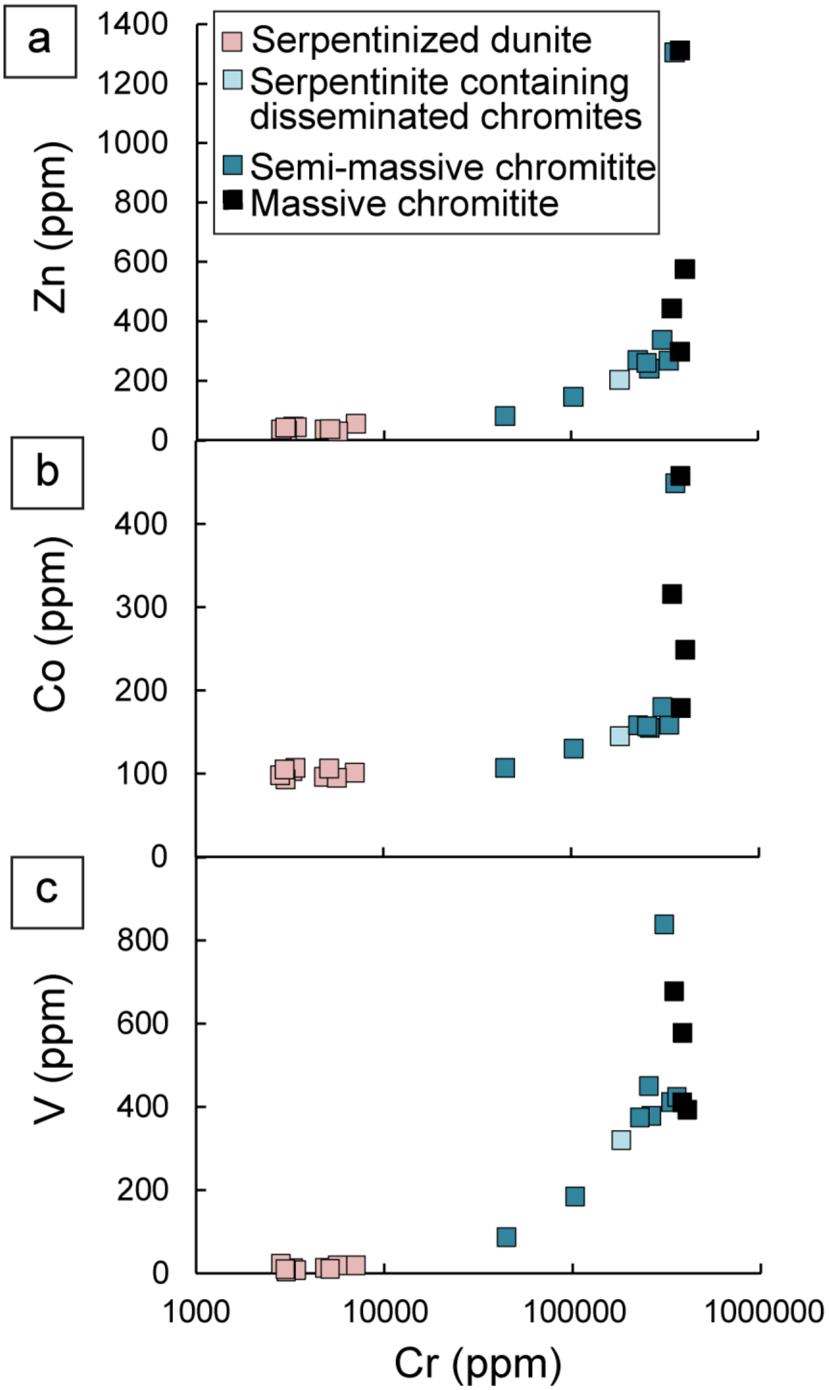
a
b
c
Serpentinized dunite
Serpentinite containing disseminated chromites
Semi-massive chromitite
Massive chromitite
Zn (ppm)
0
200
400
600
800
1000
1200
1400
Co (ppm)
0
100
200
300
400
V (ppm)
0
200
400
600
800
1000
10000
100000
1000000
Cr (ppm)

Fig. 9.

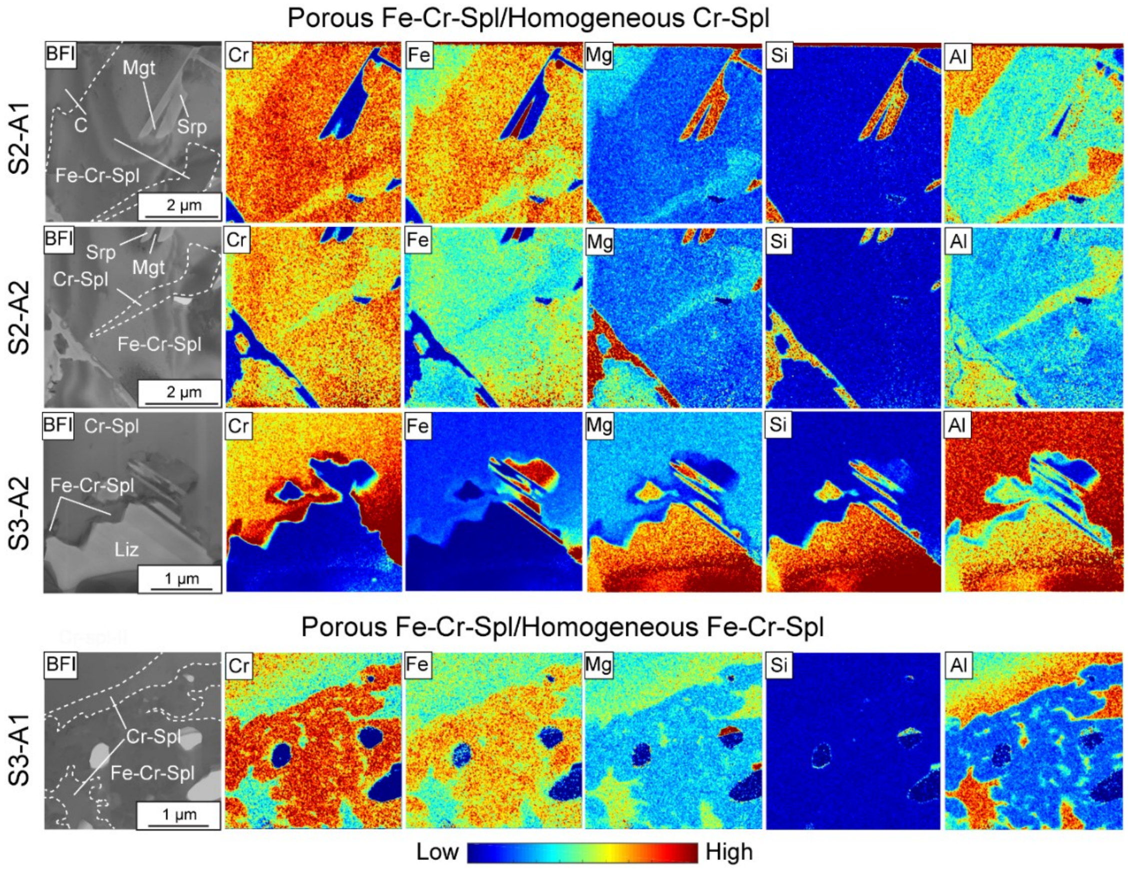
Porous Fe-Cr-Spl/Homogeneous Cr-Spl
S2-A1
BFI
Mgt
C
Srp
Fe-Cr-Spl
2 μm
Cr
Fe
Mg
Si
Al
S2-A2
BFI
Srp
Mgt
Cr-Spl
Fe-Cr-Spl
2 μm
Cr
Fe
Mg
Si
Al
S3-A2
BFI
Cr-Spl
Fe-Cr-Spl
Liz
1 μm
Cr
Fe
Mg
Si
Al
Porous Fe-Cr-Spl/Homogeneous Fe-Cr-Spl
S3-A1
BFI
Cr-Spl
Fe-Cr-Spl
1 μm
Cr
Fe
Mg
Si
Al
Low
High

Fig. 10.

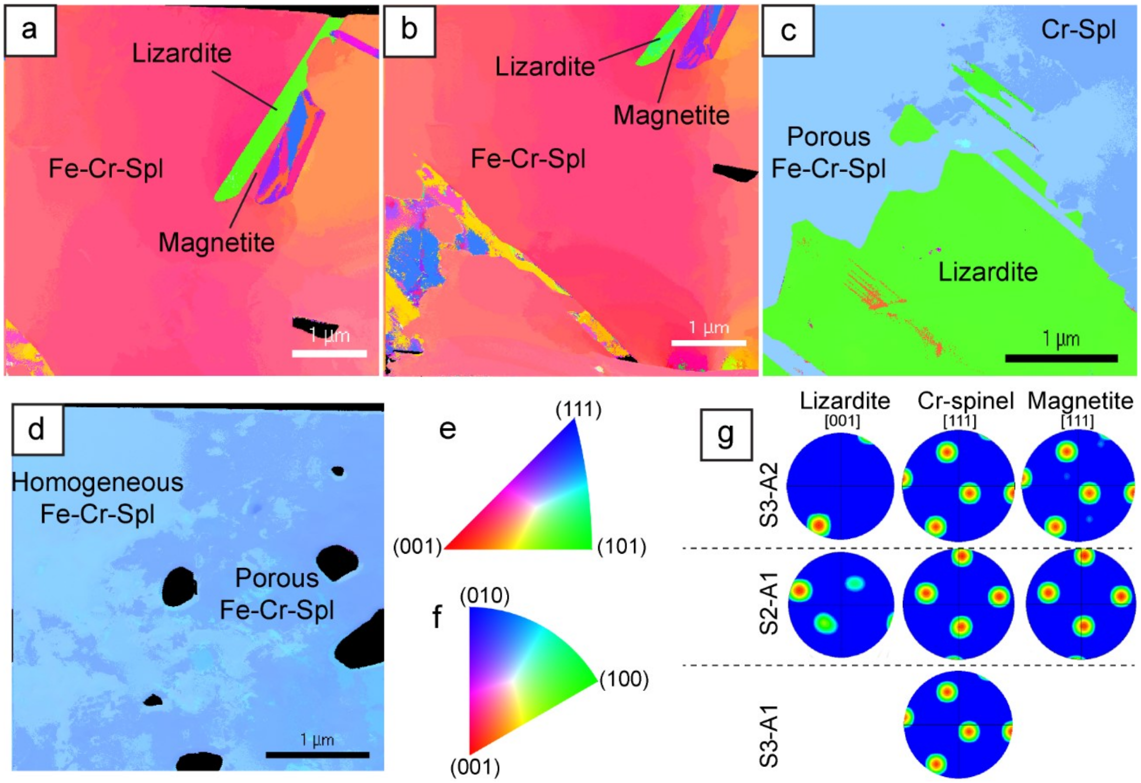
a
Lizardite
Fe-Cr-Spl
Magnetite
1 µm
b
Lizardite
Magnetite
Fe-Cr-Spl
1 µm
c
Cr-Spl
Porous
Fe-Cr-Spl
Lizardite
1 µm
d
Homogeneous
Fe-Cr-Spl
Porous
Fe-Cr-Spl
1 µm
e
(111)
(001)
(101)
f
(010)
(100)
(001)
g
Lizardite
[001]
Cr-spinel
[111]
Magnetite
[111]
S3-A2
S2-A1
S3-A1

Fig. 11.

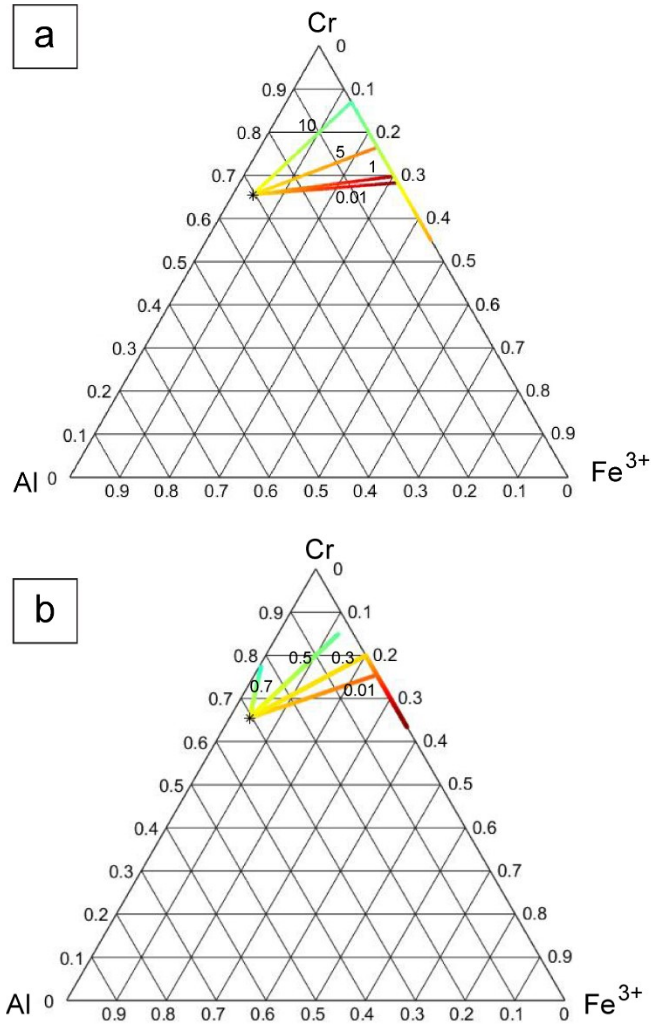

Fig. 12.

Table 1. Serpentinized dunite mineral modes (wt.%) and X_{Mg} of olivine were retrieved from least-square (LSQ) regression through the bulk dunite composition

Sample No.	**Deposit name**	**X_{Mg} Ol**	**Chr (wt.%)**	**Srp (wt. %)**
KA3-5	Kalchenari-3	92.9	1.8	78.3
HA2-2a	Haj-Ghasem	90.5	1.5	80.4
SI-2b	Main Sinerkar	89.5	0.2	81.5
O1	Olang-Sir	93.8	0.9	80
EB-3	Ebrahim	90.5	1.6	78.7
KE-3	Kermaniha Tunnel	92.3	1.2	79.5

IM-2	Imam Hossein	91.7	0.7	80.3
O24	Olang-Sir	88.1	0.5	82.9
O26	Olang-Sir	91.8	0.7	80.9

Table 2. Chromitite mineral modes (wt.%) retrieved from LSQ regression through the chromitite bulk rock composition

Sample No.	**Deposit name**	**Texture**	**X_{Mg} Ol**	**Spinel (wt.%)**
SI-2c	Sineh-Kar	Semi-massive	-	80.3
KA3-1c	Kalchenari-3	Semi-massive	93.8	70.9
HA2-1	Haj-Ghasem	Semi-massive	-	86.8
KA1-1b	Kalchenari-1	Semi-massive	93.8	68.5
KE-2	Kermaniha Tunnel	Semi-massive	92.5	67.8
KA5-1a	Kalchenari-5	Disseminated	93.4	53.7